Research Square

Preprints are preliminary reports that have not undergone peer review.
They should not be considered conclusive, used to inform clinical practice,
or referenced by the media as validated information.

Effects of Particle Size and Functional Group on Spent Engine Oil and Diesel Adsorption by Corncob– Groundnut Shell Nanobiocomposite: A Study for Potential Application in Bioremediation

Sixtus Eko Alexander

alexsixalex784@gmail.com

University of Ibadan

Mohammed Abdullahi Evuti

University of Abuja

Bala Isah Abdulkarim

University of Abuja

Abdulwasiu Abdurrahman

University of Abuja

Kamiludeen Olanrewaju

University of Abuja

Abdullahi Zakari

University of Abuja

Research Article

Keywords: Adsorption, Corncob, Groundnut Shell, Nanobiocomposite, Spent Engine Oil, Hydrocarbon Remediation

Posted Date: November 20th, 2026

DOI: https://doi.org/10.21203/rs.3.rs-11511516/v1

License: This work is licensed under a Creative Commons Attribution 4.0 International License.
Read Full License

Additional Declarations: No competing interests reported.

Research Article

Effects of Particle Size and Functional Group on Spent Engine Oil and Diesel Adsorption by Corncob–Groundnut Shell Nanobiocomposite: A Study for Potential Application in Bioremediation

[1*]Sixtus Eko Alexander, [1]Mohammed Abdullahi Evuti, [1]Bala Isah Abdulkarim, [1]Abdulwasiu Abdurrahman, [2]Kamiludeen Olanrewaju, and [2]Abdullahi Zakari

[1]Department of Chemical Engineering, University of Abuja, FCT Abuja, Nigeria.
[2]Department of Nuclear Engineering, University of Abuja, Abuja-FCT, Nigeria.
**Corresponding author's email: alexsixalex784@gmail.com*

Abstract

Spent engine oil and diesel are persistent hydrocarbon pollutants. In bioremediation, corncob and groundnut shell have each been applied as biosorbents/biostimulants, but how particle size and functional chemistry govern the performance of their combined biocomposite towards spent engine oil and diesel bioremediation remains poorly understood. This study investigated the influence of particle size and functional chemistry of a 1:1 corncob–groundnut shell biocomposite on the adsorption of spent engine oil and diesel. Corncob and groundnut shell were processed into macro-, micro-, and nano-sizes through mechanical milling and characterized using FTIR, SEM–EDX, DLS, BET surface area analysis, and XRD. The DLS analysis showed a reduction in average particle size from 438.4 d.nm to 45.81 d.nm, while BET analysis reported a specific surface area of 252.67 $m^2 g^{-1}$, BJH analysis reported mesopore diameter of 2.115 nm for the nanobiocomposite. SEM images indicated reduced porosity and surface roughness with decreasing particle size, XRD analysis revealed progressive amorphization of the biocomposite following milling. Adsorption experiments demonstrated that pollutant removal efficiency increased significantly with decreasing particle size. By linking particle-size reduction to measurable gains in surface area and removal efficiency, this work provides a basis for designing bio-based adsorbents for petroleum hydrocarbon remediation.

Keywords: Adsorption, Corncob, Groundnut Shell, Nanobiocomposite, Spent Engine Oil, Hydrocarbon Remediation.

1.0 Introduction

Spent engine oil and diesel are major sources of hydrocarbon pollution in aquatic and mainly terrestrial environments [1]. Their indiscriminate disposal introduces toxic organic compounds, polycyclic aromatic hydrocarbons (PAHs), heavy metals, and other persistent pollutants into ecosystems, leading to reduced soil fertility, groundwater contamination, and ecological damage [2-4]. Consequently, developing efficient, sustainable, and cost-effective remediation technologies has become an environmental priority. Conventional physical, chemical, electrical, and thermal remediation methods are generally rapid but are often expensive, site-specific, energy-intensive, environmentally intrusive, or require sophisticated equipment and

additional treatment processes [2, 5-8]. Their major limitations include high cost of implementation, low efficiency, limited versatility, and interference from other environmental constituents [8]. Bioremediation has emerged as a more economical and environmentally friendly alternative, despite its relatively slower rate [9-11]. It uses living organisms to detoxify and restore environments contaminated by petroleum products and has gained widespread acceptance because of its simplicity, high removal efficiency, low energy demand, and adaptability to diverse contaminants [2]. The success of bioremediation largely depends on adsorbent properties such as surface area, pore structure, particle size distribution, and surface functional groups, which control the availability of active adsorption sites [2]. Adsorption equilibrium also plays a crucial role in pollutant removal by governing biomolecule–surface interactions, while environmental factors including pH, temperature, and ionic strength influence these processes [12–14].

Agricultural residues are promising low-cost candidates for such adsorbents. Corncob and groundnut shell are non-toxic, biodegradable agricultural residues with favourable physicochemical properties, including good moisture retention and pH values ranging from neutral to slightly acidic/basic, making them suitable for support of microbial activity and environmental applications [15, 16]. Corn is one of the world's major agricultural crops, with corncobs and husks constituting about 20–30% of the plant biomass [17]. Corncobs contain about 27.71% cellulose, 38.78% hemicellulose, and 9.4% lignin [18, 19]. Similarly, groundnut shells possess high porosity and carbon content, comprising about 34–45% cellulose, 12–16% hemicellulose, and 27–33% lignin [20] (the dry materials are shown in Figures 1 and 2, Section 2.0).

Both materials therefore contain crystalline cellulose and amorphous hemicellulose and lignin [21, 22], while silica present in their ash may also exist in an amorphous form. Cellulose and hemicellulose are generally neutral to slightly acidic, whereas lignin exhibits acidic characteristics due to its functional groups and acid-releasing tendency during degradation [23].

The cellulose, hemicellulose, and lignin in these materials contain abundant oxygen-bearing functional groups that interact with hydrocarbons through adsorption, hydrophobic attraction, and surface complexation [24–26]. Their surface area and functional chemistry determine the availability of active binding sites, thereby enhancing pollutant adsorption, degradation, and heavy metal immobilization [27]. These characteristics underpin their potential as sustainable adsorbents and form the basis of this study.

Corncobs show high adsorption performance for removing hydrocarbons, oils, and grease from water and soil [28]. Research has shown that raw and modified corncob materials remove up to 85% to over 94% of total oil, grease, and petroleum hydrocarbons from wastewater or washing effluents [28-30], and groundnut (peanut) shells effectively adsorb hydrocarbons, such as crude oil and oil spills from water, because the natural material is both oleophilic (oil-attracting) and hydrophobic (water-repelling) [31]. Nonetheless, their potential application in bioremediation of petroleum and its byproducts such as spent engine oil and diesel has not been explored. Smaller groundnut shell particles (under 150 μm) provide a higher surface area and show a greater affinity for oil absorption over time [32]. While raw or carbonized ground nut shells reduce oil and grease in wastewater, standalone adsorption may leave residual hydrocarbons above strict regulatory discharge limits, meaning they work best as part of an integrated treatment system [30].

Sixtus *et al*. [10] investigated the efficacy of a corncob–groundnut shell biocomposite in remediating soils polluted with spent engine oil and grease. However, they did not evaluate the influence of surface characteristics, functional chemistry, or adsorption capacity, which are critical to bioremediation efficiency. While the study of Marvin *et al.* [32] concluded that corncob and groundnut shell are effective and sustainable adsorbents for produced water treatment and could serve as economical alternatives for petroleum-wastewater management in the petroleum industry and previous studies demonstrating the synergistic use of corncob and groundnut shell as adsorbents for environmental remediation [10, 33], limited information is available on the synergistic capacity of corncob-groundnut shell with focus on combined effects of particle-size reduction, structural modification, surface-area enhancement, and functional-group availability on the adsorption of spent engine oil and diesel. In addition, the effect of nanosynthesis on the adsorption behaviour of corncob–groundnut shell biocomposites remains poorly understood.

The novelty of this study lies in three aspects. First, it evaluates a 1:1 corncob–groundnut shell biocomposite prepared at macro-, micro- and nano-scale as an adsorbent for spent engine oil and diesel, a combination for which little information is available. Second, it relates adsorption performance directly to measured particle size, surface area, pore structure, crystallinity and functional chemistry. Third, it interprets the adsorption mechanism using the Freundlich isotherm. The objectives were therefore to (i) prepare macro-, micro- and nano-sized corncob–groundnut shell adsorbents by mechanical milling; (ii) characterize them by FTIR, SEM–EDX, DLS, BET and XRD; (iii) determine the removal efficiency of each size fraction for spent engine oil and diesel; and (iv) provide deeper insight into the design of efficient bio-based adsorbents for petroleum hydrocarbon remediation.

2.0 Materials and Methods

Sourcing of Precursors

The groundnut shell and corncob were sourced from Gwagwalada market, FCT, Nigeria (Figures 1 and 2).



Figure 1: Dry Groundnut Shell



Figure 2: Dry Corncob

The spent engine oil and diesel pollution soil (with minimal traces of grease) was sourced from the main campus senate building generator house of University of Abuja, FCT, Nigeria (Location: latitude 8.981100, longitude 7.179999) – as shown in Figure 3.

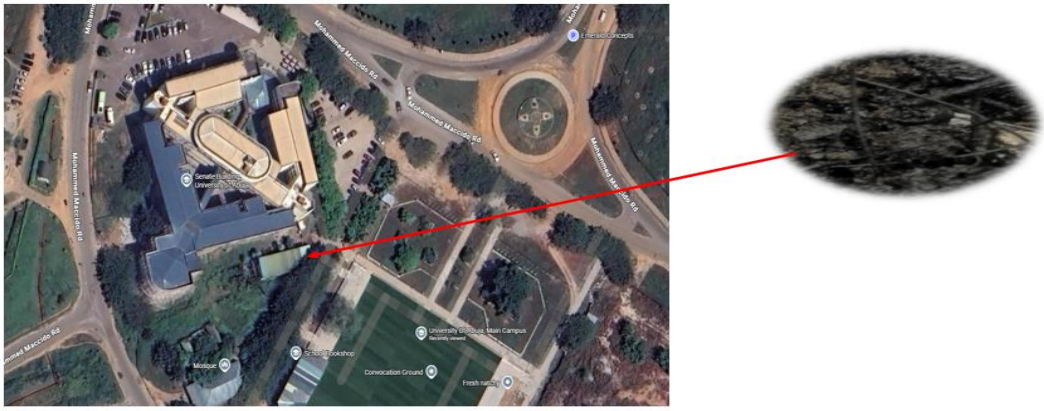

Figure 3: Map of the University of Abuja, Nigeria
(Pointer showing the Generator house point of pollution)

Physicochemical analyses of Adsorbent (Corncob and Groundnut Shell)

pH Analysis, Bulk Density and Electrical Conductivity.

The pH (using Jenway model 3015 digital pH meter), bulk densities and electrical conductivity of spent engine oil and diesel, corncob and groundnut shell were analyzed using the method adopted by Sixtus *et al.* [34].

Synthesis, Surface Characterization and Adsorption Study of Groundnut shell and Corncob

Nanosynthesis and compositional analysis of Dried Groundnut Shell and Corncob

The nanosynthesis was carried out using ball mills. The milling was carried out at the speed of 300 rpm, with a ball to powder ratio of 10:1 following previous works of Fukushima *et al.* [35] and Yaro *et al.* [36]. From FTIR analysis, the method proposed by Van Soest and Robertson [37] was used to decode the lignin, cellulose, and hemicellulosic concentrates in the adsorbent.

Scanning Electron Microscopy – Energy Dispersive X-Ray (SEM-EDX) Spectroscopy and Dynamic Light Scattering (DLS) Analysis

The morphology of the adsorbent of different sizes after the synthesis processes was studied. The morphological modifications were studied by taking SEM images at same magnification of all size categories of the adsorbent [38]. DLS analysis was used to ascertain the average size of synthesized adsorbent before and after synthesis process [38].

X-Ray Diffractometry (XRD) Analysis of Nanosynthesized Adsorbent

According to the procedure proposed by Harrington and Santiso [39] and Thota *et al.* [40], wide-angle X-ray diffraction (PANalytical, Xpert PRO) was used to estimate the crystallinity of powdered groundnut shell and corncob. The resulting data was then analyzed using the methods proposed by Harrington and Santiso [39] and Holder and Shaak [41].

Lignocellulosic Chemometric Analysis of Adsorbents

The sourced groundnut shell and corncob were pounded to smaller pieces, dried at 60ºC and milled. Cellulose, hemicellulose, and lignin contents were determined adopting the method of Van Soest and Robertson [37] in estimating the neutral detergent fibre (NDF), acid detergent fibre (ADF) and acid detergent lignin (ADL).

Phase Separation and Adsorption Study: Comparative Surface Adsorption Study Using Ultraviolet-Visible Light (UV-Vis) Spectrometric Analysis for Concentration Determination.

Prior to nanosynthesis of the precursors, corncob (CC) and groundnut shell (GS) were processed into three distinct size ranges by mechanical grinding machine: macro, micro and nano, and all three particulate groups were used in an adsorption study.

Phase Separation and Adsorption Study

Oil and water are generally immiscible and as a result hardly form a single phase at room temperature. Solvent extraction method was applied in oil recovery from polluted soil for the adsorption study. Three (3) liters of distilled water (at a temperature of 80°C) was poured into 1kg of the polluted soil (average temperature of 30°C) to create an Oil-in-water (O/W) emulsion after which the mixture was allowed to stand alone for 24 hrs after about 5 mins of mild shaking and stirring. The heated water increased the potential for oil stripping from the polluted soil in an oil-wet polluted soil. The oil from polluted soil was seen in the solvent (water) and until at the end of the 24 hrs, three distinct layers of: sediment, water and oil were observed with a clear water-oil contact – sediment collected at the bottom, oil at the top and water between them. Using a separating funnel the water and oil were separated and heated and temperature was kept steady at 25°C to remove residual water from the oil phase (adsorbate) [34]. This experiment was done quadruplicate to enable enough of spent engine oil and diesel being stripped.

Adsorption Study

To study the effectiveness of the adsorption as a result of changing particle sizes, macro-sized, micro-sized and nano-sized adsorbents containing CC+GS in the ratio 1:1 were prepared, with the adsorbate (spent engine oil and diesel extracted from polluted soil). In this work, macro-sized denotes particles larger than 100 µm, micro-sized denotes sub-micrometre particles with a Z-average of 438.4 d.nm, and nano-sized denotes particles with a Z-average of 45.81 d.nm. Typically, adsorbent dosage ranges from 0.5 g/L to 10 g/L of solution (or adsorption complex) [42, 43]. Three adsorption complexes of each made up 100mg of the three adsorbents in 100mL of adsorbate was prepared and agitated at 150rpm for 1min in every 10mins (under room temperature of 31°C). Agitation was to enable the formation of a homogenous mixture and increase surface interaction between adsorbent and adsorbate. Taking note of retention times (10mins interval), environmental and system's temperature, UV-Vis spectrometer was used at the end of every 10mins to analyze the concentrations of adsorbate attached to adsorbent surface according to the method proposed by Sixtus *et al.* [34].

Density Determination

Following the method proposed by Bakovets and Konicheva [44], a clean, dry graduated cylinder placed on a weighing balance and tared. 50ml of the extracted spend engine oil and diesel was then poured into the cylinder, ensuring the reading was taken at the bottom of the meniscus at eye level. The weight of the cylinder containing spent engine oil and diesel was recorded and the mass difference between the mass of the empty cylinder and was subtracted

from the mass of spent engine oil and diesel in cylinder weighed to get the mass of the spent engine oil and diesel alone. The density of spent engine oil and diesel was calculated thus:

$$\rho_{SE\&G} = \frac{M_{SE\&G}}{V_{SE\&G}} = \frac{M_{C+SE\&G} - M_C}{V_{SE\&G}} \quad (1)$$

Where (Mass of spent engine oil + diesel) = (Mass of cylinder and spent engine oil and diesel) – (Mass of empty dry cylinder).

$V_{SE\&G}$ = Measured volume of spent engine oil and diesel in graduated cylinder; and

$\rho_{SE\&G}$ = Calculated density of spent engine oil and diesel.

3.0 Results and Discussion

Physicochemical Analysis of Soil Samples

Physicochemical analysis of soil samples collected at point B (as shown in Figure 3) is the polluted soil sample. The results of the physicochemical analysis of spent engine oil and grease from polluted soil sample is shown in Table 1.

Table 1: Physicochemical Analysis of Spent Engine oil and Diesel extracted from pollution soil.

Parameter (Unit)	Value
pH	5.32
Oil and Diesel Conc. (mg/l)	13487
Conductivity (dS/m)	0.9779

pH and Conductivity

Prior to pH determination, the soil sample from location B was gently stirred to improve homogeneity. The pH of each sample was measured in triplicate at 5-min intervals between successive measurements at room temperature (28 °C). The recorded pH values were 5.32, 5.33, and 5.32, respectively, and the mean value was calculated and used as the representative pH for each sample. The observed variation between replicate measurements was ≤ ±0.01 (0.19% error), indicating good measurement consistency.

Electrical conductivity (EC) was also determined to assess the ionic characteristics of the soil samples. In general, soil electrical conductivity increases with the concentration of soluble ions and other charged constituents present in the soil matrix. Elevated EC values may therefore indicate increased concentrations of dissolved salts or ionic contaminants, including certain heavy metals.

Following gentle stirring to ensure adequate homogenization, EC measurements were performed in triplicate at room temperature (27 °C), with a 5-min interval between successive measurements. The recorded values were 0.9779, 0.9779, and 0.9778 dS/m, respectively. The mean value was calculated for the sample, with a maximum deviation of ≤ ±0.0004 dS/m (0.041% error), demonstrating high consistency among the replicate measurements.

Physicochemical Analysis of Corncob and Groundnut Shell

The physicochemical properties of the stimulants were analyzed. The Properties of the stimulants (corncob and groundnut shell) are shown in Table 2.

Table 2: Properties of Corncob and Groundnut Shell

Parameter	Before Nanosynthesis (Size ~ 10mm)		After Nanosynthesis (Size ~ 65nm)	
	Granulated Corncob	Granulated Groundnut Shell	Powdered Corncob	Powdered Groundnut Shell
pH	8.41	7.63	8.39	7.40
Bulk Density (g/cm^3)	0.8	0.78	1.25	1.17

Bulk Density

The bulk density of the stimulants is affected by the mass of the stimulant and its volume. The recorded bulk density of corncob and groundnut shell were $0.8g/cm^3$, and $0.78\ g/cm^3$ respectively. However, after nanosynthesis the bulk density recorded was $1.25g/cm^3$ and $1.17\ g/cm^3$ respectively. This is because the ball milling process reduced volume while keeping mass constant.

pH

After mild stirring (to increase homogeneity), pH measurement was taken thrice for each sample at 5minutes interval between successive tests and obtained the results consecutively: corncob before nanosynthesis (8.41, 8.41 and 8.41); corncob after nanosynthesis (8.39, 8.40, and 8.39); groundnut shell before nanosynthesis (7.63, 7.63, and 7.63); groundnut shell after nanosynthesis (7.40, 7.40, and 7.40); at room temperature of 27ºC and an average value was recorded for each of the samples. Deviation recorded was $\leq (\pm 0.01)$. Decreasing particle size generally increases surface area. This increased surface area allowed for more frequent interactions with surrounding molecules of the system. Hence, decreasing the particle size of corncob and groundnut shell led to increased solubility. Thermodynamically, this is due to the exposure of acidic/basic functional groups that were previously trapped inside the crystalline structure of the raw biomass. However, they were exposed to the water interface as a result of nanosynthesis.

Corncob and Groundnut Shell Compositional Analysis

Cell walls are predominately composed of cellulose, hemicellulose and lignin. Table 3 highlights the results from the analysis to quantitatively verify the NDF, ADF, ADL contents in the groundnut shell and corncob used in the experiment.

Table 3: NDF, ADF, ADL, cellulose and hemicellulose contents of groundnut shell and corncob by weight sourced from Gwagwalada Market, Abuja.

S/N	Adsorbent	Mean Value of Compositional Qualities (g/kg of adsorbent)				
		NDF	ADF	ADL (Lignin)	Cellulose	Hemicellulose

1	Corncob	715.0	340.0	87.0	253.0	375.0
2	Groundnut Shell	829.0	710.0	292.0	418.0	119.0

Higher lignin content was observed in groundnut shell (29.2%) compared to that in in corncob (12.2%). High lignin content generally translates to higher adsorption capacity for many organic pollutants and heavy metals, along with a slower degradation rate of the adsorbent material. Lignin contains many functional groups like phenols (C_6H_5OH), methoxyls (–OCH_3), and carboxyls (–COOH) – groups that attract and hold chemical pollutants [10].

Surface Characterization of Groundnut Shell and Corncob

Determination of Average Particle Size from Differential (or Dynamic) Light Scattering (DLS) Analysis

To eliminate the effects of multiple light scattering, the samples particle concentration was maintained within an appropriate measurement range. The concentration range was typically established prior to analysis by systematically diluting the samples and evaluating the consistency of the resulting measurements. The suitable concentration range was identified when further dilution produced no significant variation in the measured particle size or intensity distribution. The lower concentration limit was primarily determined to ensure that light scattered by the dispersion medium and any extraneous particles did not interfere with the measurement. Ideally, the scattering signal originating from the dispersant used for sample dilution was sufficiently weak to avoid compromising the accuracy and reliability of the results. In the present study, dynamic light scattering (DLS) analysis was performed using distilled water as the dispersant, and the parameters and results obtained are summarized in Table 4.

Table 4: Results from Dynamic Light Scattering (DLS) Analysis before and After Nanosynthesis of Groundnut Shell and Corncob.

Details	Property (unit)	Quantity/Description
Sample	Dispersant	Fresh Distilled Water
	Dispersant R.I	1.330
	Viscosity (cP)	0.8872
	Material R.I	1.59
	Material Absorption	0.010
System	Temperature (°C)	25
	Count Rate (kcps)	209.9
	Duration Used (s)	70
	Cell Description	Disposal Sizing Cuvette
	Attenuator	7
Results	PdI	0.231
	Intercept	0.757
	Result Quality	Good

The DLS analysis measured the average hydrodynamic particle size and the broadness of the size distribution of submicron particles dispersed in water having a refractive index (R.I) of 1.330, viscosity of 0.8872 cp at a temperature of 25°C. For both DLS analysis (i.e. before and

after nanosynthesis) the dispersant characteristics as well as that of adsorbent and product remained the same – with R.I of 1.59 and material absorption of light being 0.010. Intensity fluctuations of the scattered light can be evaluated either as a time-dependent phase shift or as a spectral frequency shift. Scattering intensity/count rate which is the intensity of the light scattered by the particles in the scattering volume as measured by a detector was measured at 209.9 kcps for a duration of 70s. The test report includes the scattered light intensity-weighted harmonic mean particle diameter (Z-average, d.nm) and polydispersity index (PdI) – a dimensionless measure of the broadness of the particle size distribution. DLS analysis of adsorbent before nanosynthesis, using water as the dispersant, and the results obtained are summarized in Table 5:

Table 5: Results before Nanosynthesis (Z-average = 438.4 d.nm)

Size Distribution Report	Recorded Peak	Size (d.nm)	Percentage (%)	St. Dev. (d.nm)
Intensity	Peak 1	623.5	50.0	382.2
	Peak 2	157.1	41.7	53.43
	Peak 3	5356	8.3	343.5
Volume	Peak 1	908.0	58.8	420.1
	Peak 2	136.5	26.1	55.59
	Peak 3	5445	15.1	642.1
Number	Peak 1	142.3	100.0	119.0
	Peak 2	0.00	0.00	0.00
	Peak 3	0.00	0.00	0.00

DLS analysis of adsorbent after nanosynthesis, using water as the dispersant, and the results obtained were summarized in Table 6.:

Table 6: Results after Nanosynthesis (Z-average = 45.81 d.nm)

Size Distribution Report	Recorded Peak	Size (d.nm)	Percentage (%)	St Dev. (d.nm)
Intensity	Peak 1	15.45	86.6	5.455
	Peak 2	545.1	5.4	304.2
	Peak 3	158.0	4.5	63.45
Volume	Peak 1	0.8559	0.7	0.3265
	Peak 2	11.92	94.0	5.565
	Peak 3	334.0	3.8	310.0
Number	Peak 1	2.449	0.0	0.4965
	Peak 2	41.42	0.9	6.616
	Peak 3	9.612	93.4	3.154

In DLS analysis, the peaks indicate the prevalent particle sizes (i.e. the size range where most particles are present). The presence of multiple peaks suggests a mixture of different particle sizes or the presence of aggregates. Their relative percentages reflect the distribution's contribution to the total, and standard deviation (St. dev.) quantifies the dispersion or broadness of the distribution, with higher values indicating greater variability.

Particle Size Distribution

Submicron-sized particles suspended in the liquid medium (water), remained in continuous and random motion due to Brownian motion. When the suspension was illuminated with a laser beam, the particles scattered light, producing temporal fluctuations in the detected scattering intensity as a consequence of their diffusive motion. While DLS intensity-weighted particle size distribution measured the primary output of the measurement, using photon correlation spectroscopy (PCS), the intensity of light scattered by particles within the defined scattering volume was detected and quantified as photon pulses per unit time, typically reported as counts per second (cps). Also, the volume distribution which signifies the percentage of the total particle volume contributed by particles of a specific size was measured. The size distribution by number showed the percentage of particles within each size, where each particle has equal weight, particularly useful when the number of individual particles, and not their size-weighted contribution, is more relevant to the application. Figure 4-9, illustrates the size distributions from DLS analysis.

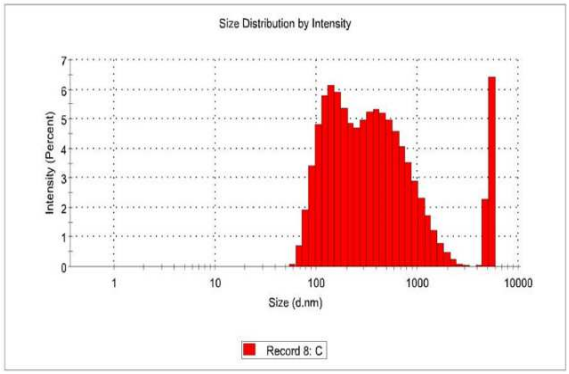

Figure 4: Size Distribution by Intensity before milling

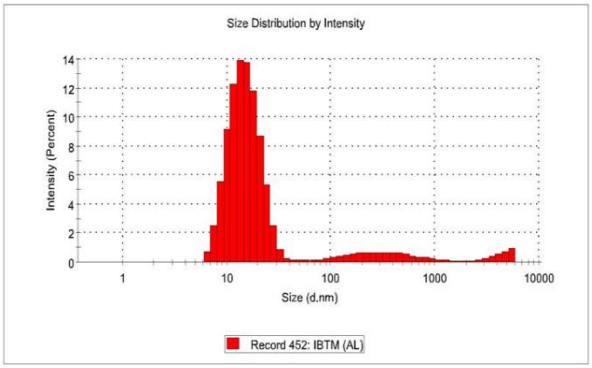

Figure 5: Size Distribution by Intensity after milling

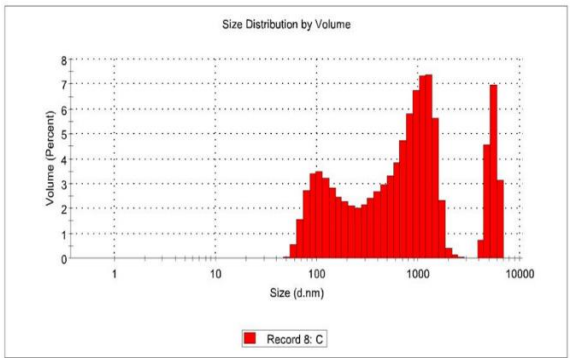

Figure 6: Size Distribution by Volume before milling

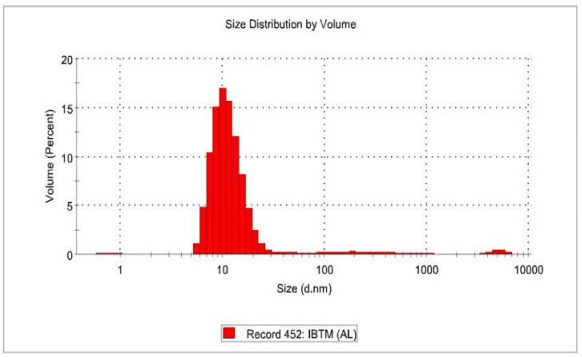

Figure 7: Size Distribution by Volume after milling

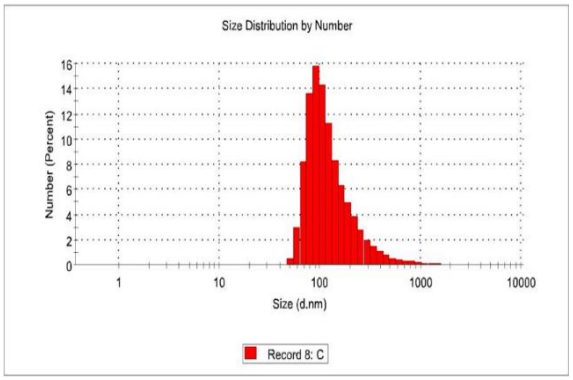

Figure 8: Size Distribution by Number before milling

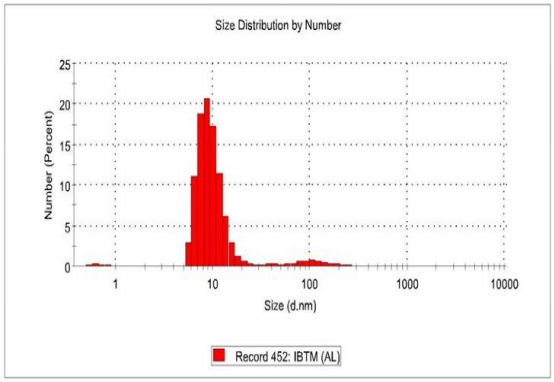

Figure 9: Size Distribution by Number after milling

Figures 4, 6 and 8 shows a size distribution by intensity, volume and number on vertical axis against size (in d.nm) on horizontal axis before nanosynthesis respectively; Figures 5, 7 and 9 respectively shows a size distribution by intensity, volume and number on vertical axis against size (in d.nm) on horizontal axis after Nanosynthesis in the DLS analysis. From Table 5, it was observed that a bulk of the particle sizes were above specification size (>100nm) considering the particle size and the St. dev indicating wide spread of data, with values that are inconsistent, diverse, and differ significantly from each other (or a central tendency). However, after nanosynthesis and as observed in Table 6, a bulk of the particles were within specification size (<100nm) considering the particle size and the St. dev indicating limited spread of data, with values that are more consistent, uniform, and differ insignificantly from each other (or a central tendency). Larger particles exhibited slower fluctuations in scattered-light intensity because of their lower Brownian diffusivity, whereas smaller particles undergo more rapid fluctuations due to their greater diffusivity. This difference in particle motion accounts for the broader skewness observed in Figures 4, 6 and 8 compared to their counterpart Figures (i.e. 5, 7, and 9 respectively).

SEM-EDX Imaging

The various sizes of stimulants prepared displayed different SEM-EDX roughness and porosity as seen in Figures 10, 11 and 12.

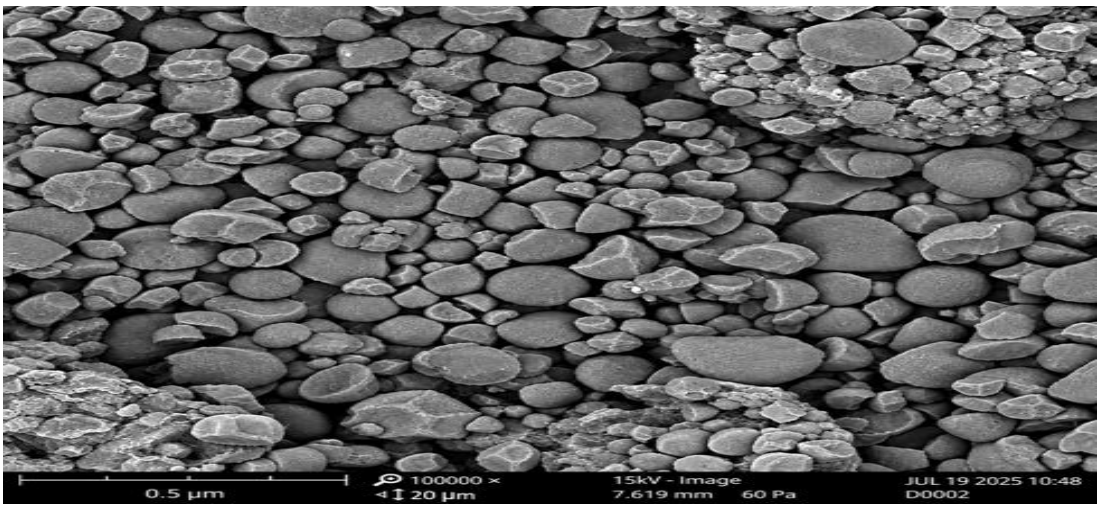

Figure 10: SEM Image of Adsorbent (Average Particle size = 45.81 d.nm) in a 1:1 mix

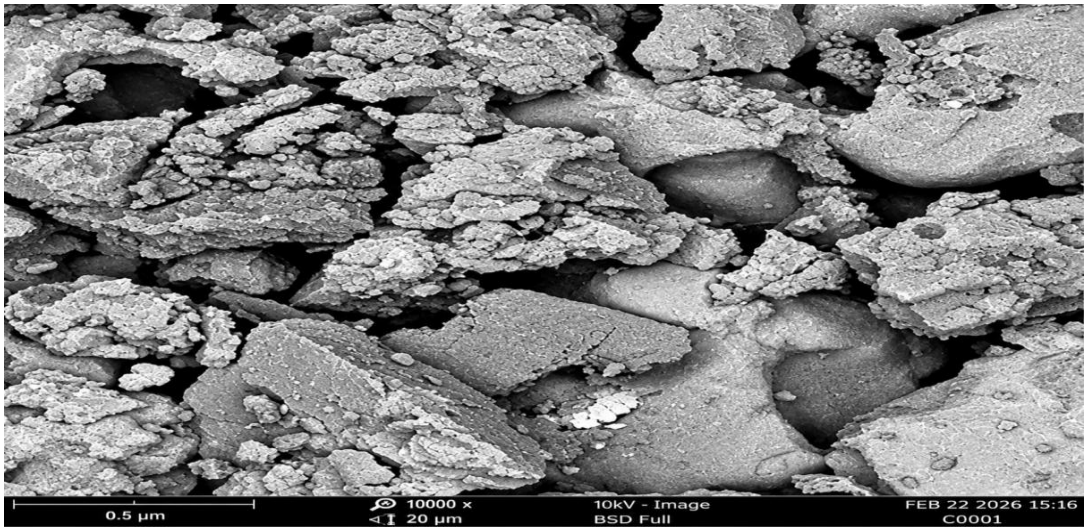

Figure 11: SEM Image of Adsorbent (Average Particle size = 438.4 d.nm) in a 1:1 mix

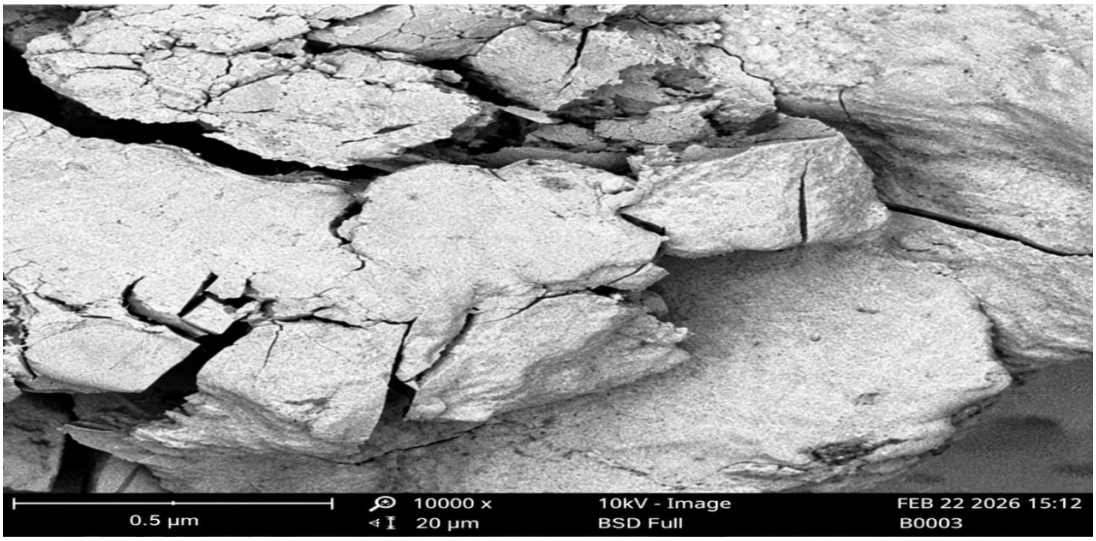

Figure 12: SEM Image of Adsorbent (Particle size ≥ 100 µm) in a 1:1 mix

SEM, when coupled with energy-dispersive X-ray spectroscopy (EDS) provided complementary evidence of interface formation in the adsorbent composites. By comparing the SEM-EDX of the different sizes of that with decreasing particulate size, surface area increases, texture exhibited more porosity indicating increased exposure of cellulosic fibers. The alteration of adsorbent particle size in the prepared samples was thoroughly studied using characterization techniques and found to be concentration specific.

Based on the results of the EDX analysis: from eleven elemental components (including C, Si, Ca, K, Cu, Sn, Ti, Fe, Mn, Cr, and N) in macro-sized adsorbent; to fifteen elemental components (C, Cu, Ag, Fe, Sn, Ba, Al, Mn, Cr, Cl, O, K, Ca, Ti, and Mg); to sixteen elemental components (C, Si, Ba, Sn, Fe, Cu, Ag, Ca, Mn, Al, K, Cl, O, Ti, Cr, and Na). Table 7 summarizes the atomic weight of the elemental components in the adsorbent as a result of ball milling.

Table 7: EDX Elemental Compositional Result in Various Sizes of the Adsorbent

Element	Element Number	Average Particle Size Distribution and Atomic Concentration of Elemental Components (ppm)		
		≥ 100 µm	**438.4 d.nm**	**45.81 d.nm**
C	6	84.43	67.42	63.08
Cu	29	1.27	4.34	1.12
Ag	47	-	2.12	0.56
Fe	26	0.65	3.36	2.34
Sn	50	0.68	1.24	1.23
Ba	56	-	0.98	1.87
Al	13	-	4.36	1.65
Mn	25	0.55	1.90	0.99
Cr	24	0.47	1.63	0.42
Cl	17	-	2.26	0.99
O	8	-	4.22	2.03
K	19	2.41	1.70	1.02
Ca	20	2.38	1.62	1.37
Ti	22	1.47	1.29	0.66
Mg	12	-	1.56	-
Si	14	5.71	-	19.72
Na	11	-	-	0.92
N	7	-	-	-

From Table 7 it can be seen that with increased milling time, and decreasing adsorbent particle size distribution carbon (C) concentration gradually fell in the biocomposite adsorbent while concentration of other components varied overtime. This experimental result shows that ball milling physically altered powder morphology, introduced the risk of contamination, and changed the relative atomic proportions measured by Energy Dispersive X-ray (EDX) spectroscopy. It generally causes changes in elemental composition, peak shifts, or the introduction of new elements.

In another view, EDX (Energy-Dispersive X-ray spectroscopy) analysis explains adsorption performance by providing elemental mapping and quantifying the chemical changes on an adsorbent's surface before and after the adsorption process. It serves as direct visual and chemical proof of whether the target pollutants were successfully captured. It served as direct visual and chemical proof of whether the target pollutants were successfully captured – consider Figures 13, 14, and 15:

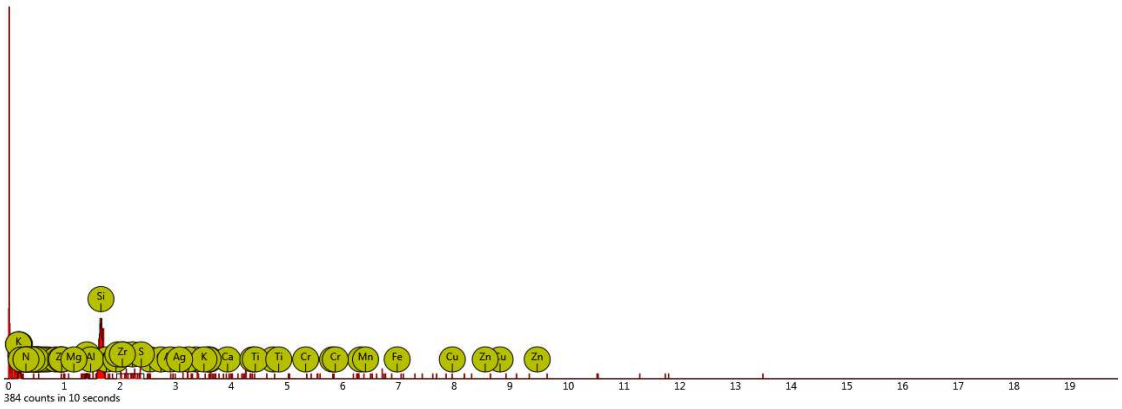

Figure 13: EDX Image of Adsorbent (Average Particle size ≈ 45.81 d.nm) in a 1:1 mix

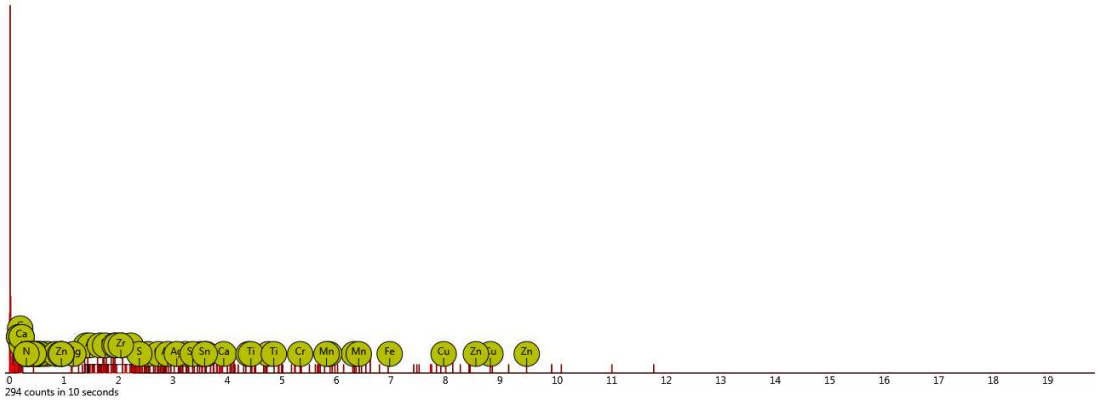

Figure 14: EDX Image of Adsorbent (Average Particle size = 438.4 d.nm) in a 1:1 mix

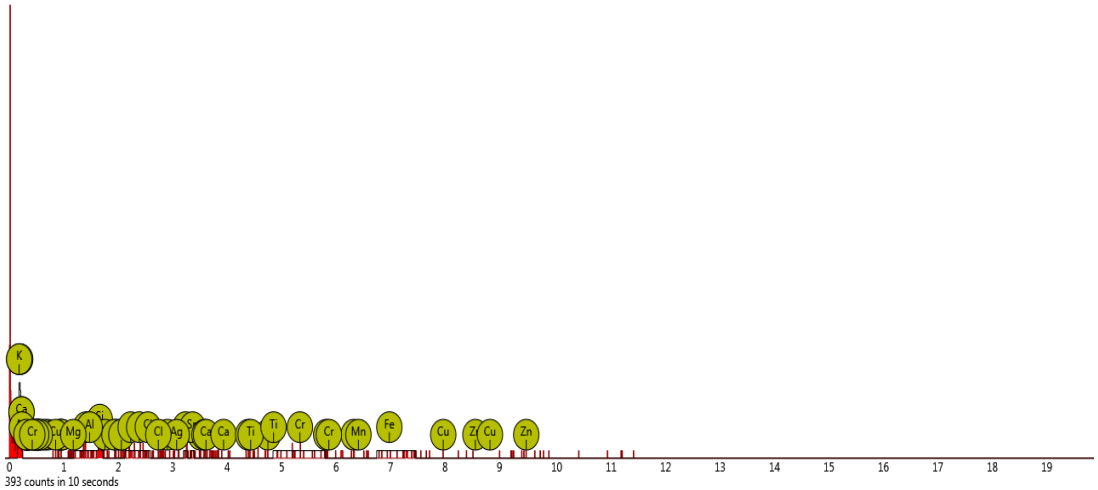

Figure 15: EDX Image of Adsorbent (Particle size ≥ 100 µm) in a 1:1 mix.

EDX analysis explained a possible adsorption performance by providing elemental mapping and quantifying the chemical changes on the adsorbent's surface before and after the adsorption process. It served as direct visual and chemical proof of whether the target pollutants could be successfully captured given the type of elements on the biocomposite – consider Figures 13, 14, and 415. The elemental tracking is a direct proof of adsorption performance with increasing surface area. Usually, EDX spectrum shows only the baseline elements of the clean adsorbent (e.g., carbon, oxygen, or silica). However, new elemental peaks appear on the spectrum corresponding to the pollutant (such as heavy metals like lead, cadmium, or arsenic). This confirms that the target molecules were physically or chemically bound to the surface. By comparing the percentage increase of the pollutant's elements on different modified adsorbents, the surface modification which yielded the highest adsorption efficiency can be determined. Based on the results of the EDX analysis as summarized in Table 7, from eleven elemental components (including C, Si, Ca, K, Cu, Sn, Ti, Fe, Mn, Cr, and N) in macro-sized adsorbent; to fifteen elemental components (C, Cu, Ag, Fe, Sn, Ba, Al, Mn, Cr, Cl, O, K, Ca, Ti, and Mg); to sixteen elemental components (C, Si, Ba, Sn, Fe, Cu, Ag, Ca, Mn, Al, K, Cl, O, Ti, Cr, and Na). The EDX was used to confirm the presence of (C=O). During the EDX, measurement different areas were focused and the corresponding peaks are shown in Figures 13, 14, and 15. Both C and O can be seen in the structures of the compositein the EDX spectrum. In spectrum

1, the quantity were (84.43), (67.42) in spectrum 2, while in spectrum 3 the values were (63.08) measured in atomic ppm for C.

The color-coded visuals show exactly where elements are located: where the pollutant elements are evenly scattered (or homogenously distributed) across the mapping image, shows the adsorbent has uniform active sites. However, where the elements cluster (or agglomerate) in specific zones, indicates uneven surface reactivity or pore clogging. This phenomenon is crucial for deciphering how the adsorption is happening. With the peak for inherent elements (like Si in Figure 13) disappearing after adsorption while other metallic peaks prove an ion-exchange mechanism occurred. Also, the surface complexion shown through an increase in specific elements (such as Zn) alongside oxygen suggests the formation of chemical complexes on the surface functional groups. Basically, nitrogen being a light element produces very weak x-ray signals which are easily absorbed or masked in EDX analysis.

Generally, crystalline nanoparticles have stronger and more uniform intermolecular (or interatomic) attractions than amorphous nanoparticles. In crystalline nanoparticles, atoms and molecules are arranged in a highly ordered, repeating lattice structure. This tight, predictable packing allows for maximum intermolecular contact and uniform bonding forces across the structure, leading to higher overall stability, greater density, and higher melting points. On the other hand, amorphous nanoparticles lack long-range order, meaning their atoms are arranged more randomly and with varying intermolecular distances. Because of this structural irregularity, the intermolecular forces holding them together are often weaker and unequal. Because amorphous nanoparticles lack strong, uniform attractive forces, they have a higher internal Gibbs free energy. This makes them thermodynamically unstable and prone to recrystallization, but it allows them to dissolve much faster and achieve greater saturation solubility than their crystalline counterparts. SEM-EDX observations revealed that as particle size decreased, surface area increased indicating increased exposure of cellulosic fibers. The alterations in the physical attributes of the prepared samples were thoroughly studied using characterization techniques and found to be concentration-specific.

Determination of Nanosynthesized Corncob and Groundnut Shell Surface Area

Brunauer-Emmett-Teller (BET) Analysis.

The raw data provided by the BET analyzer instrument is represented in Table 8:

Table 8: Pressure and Volume data from BET analysis of nanosynthesized corncob and groundnut shell biocomposite.

S/N	Relative Pressure	Volume at STP (77.350K)	1 / [V((Po/P) - 1)]
1	0.047762	13.9037	2.8864
2	0.116263	25.9665	4.0537
3	0.179468	37.1983	4.7046
4	0.241885	48.3804	5.2766
5	0.306614	60.1927	5.8779

Figures 16 and 17 are a plot of Multiple-point BET plot of on the vertical axis against relative pressure on horizontal axis and Isotherm data plot of Volume of Nitrogen at 77.350K on the vertical axis against relative pressure on horizontal axis, respectively.

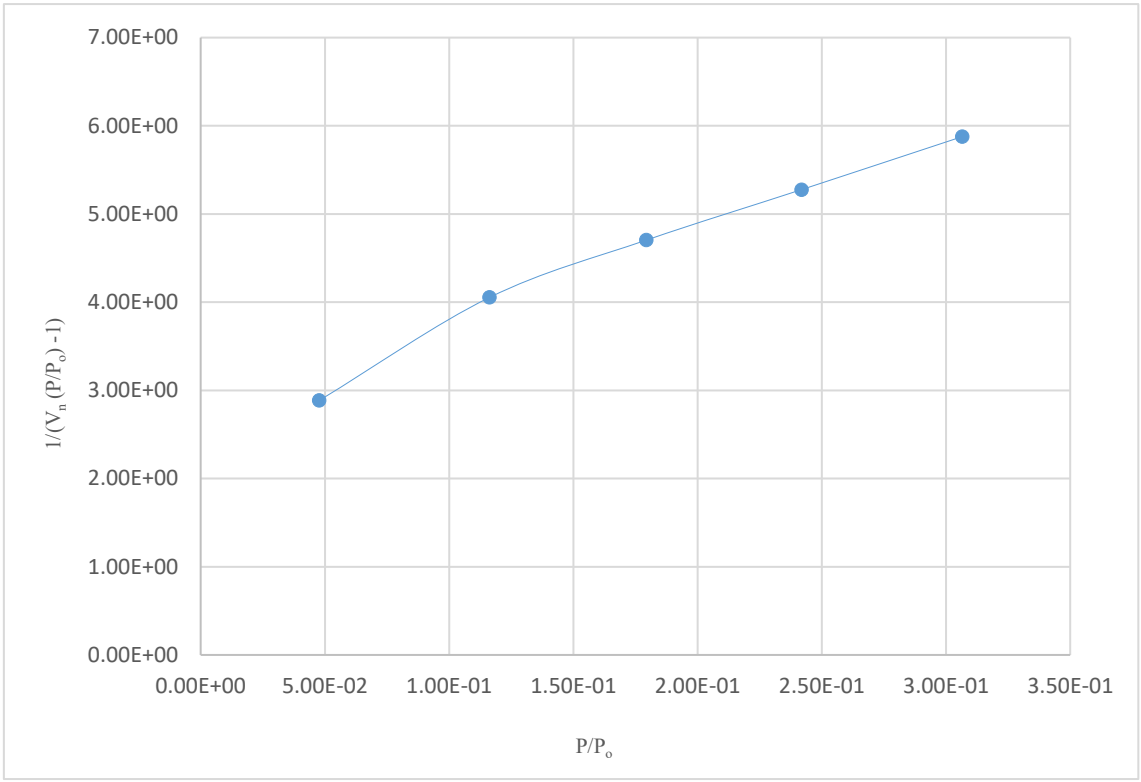

Figure 16: A Multiple-point BET plot of $1/(V_n (P/P_o) -1)$ the vertical axis against relative pressure (P/P_o) on horizontal axis.

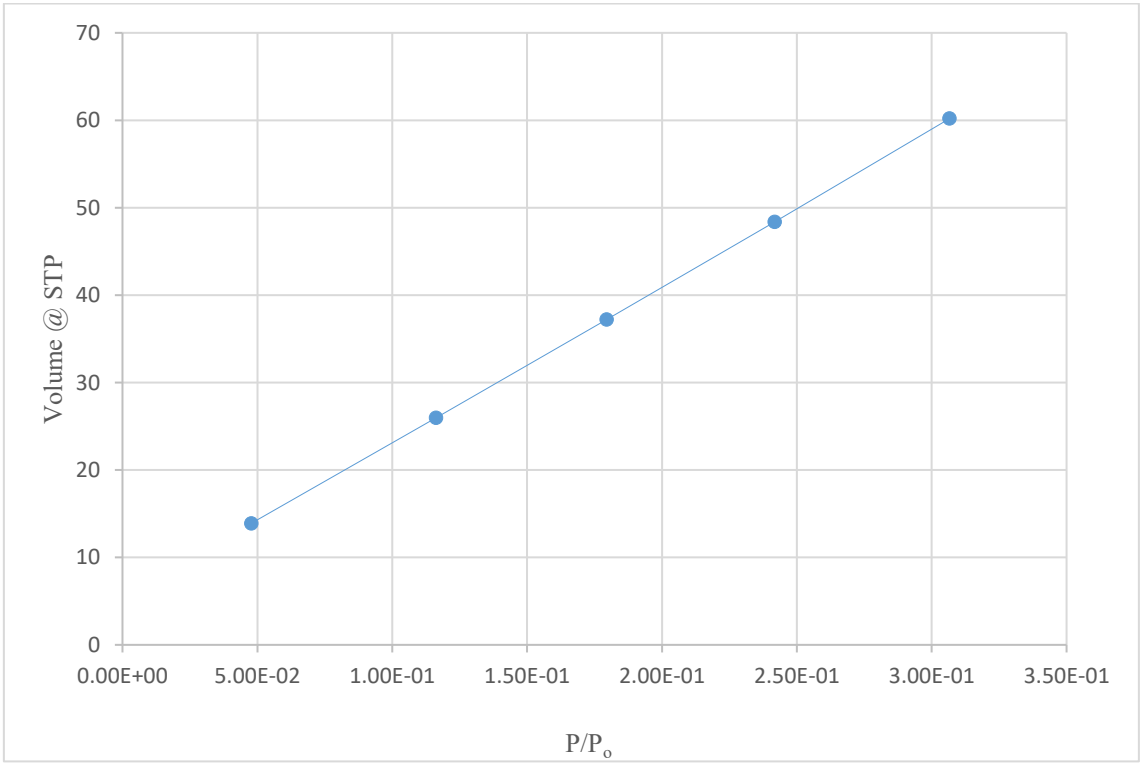

Figure 17: An Isotherm data plot of Volume of Nitrogen at 77.350K on the vertical axis against relative pressure on horizontal axis.

The instrument reported surface area of 252.669 m^2/g (Slope = 11.226, Intercept = 2.557e+00, R^2 = 0.989454, C = 5.390) for Multi-plot BET plot. However, from the Langmuir study surface area reached 724.457 m^2/g (Slope = 4.80707, Intercept = 2.79586, R^2 = 0.906). In calculating the volume specific surface area, which provides a complementary definition of nanomaterials to the arbitrary size range of 1 to 100nm, Kreyling *et al.* [45] concluded that a volume specific surface area (VSSA) greater than or equal to 60 m^2/cm^3 is a practical definition of a nanomaterial.

Three widely used approaches for evaluating sorption isotherms in relation to micropore volume and specific surface area are the Brunauer–Emmett–Teller (BET) method, the t-plot method, and the Dubinin–Radushkevich (DR) method. However, BET theory is commonly applied to determine the specific surface area of mesoporous and macroporous materials, whereas the t-plot approach distinguishes micropore filling from multilayer adsorption occurring on the external surface. In contrast, the DR method is primarily employed for the characterization and estimation of micropore volume. Although BET analysis is generally considered to be influenced by multilayer adsorption (which a more realistic compared to the Langmuir monolayer adsorption isotherm) on external surfaces and the DR approach is regarded as particularly sensitive to microporous structures, studies involving synthetic carbon materials have demonstrated that both methods can yield comparable values despite being based on different theoretical assumptions.

<u>Dubinin-Astakhov (DA) Analysis</u>

DA micropore volume and pore diameter (mode) together offer a complete blueprint of the biocomposite's sub-2nm internal pore network. Figure 18 shows the graphical relationship between pore diameter and differential pore volume of the corncob-groundnut shell nanobiocomposite:

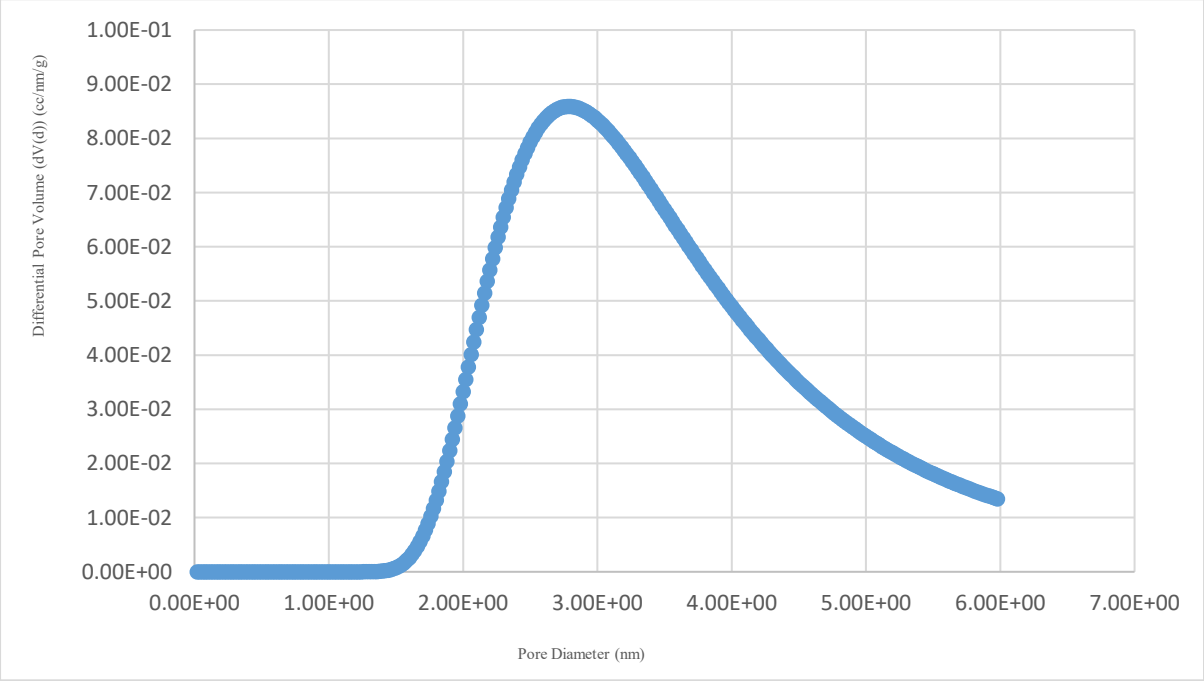

Figure 18: A plot of pore diameter versus differential pore volume

Dubinin-Astakhov (DA) Method Summary

Best E = 0.819 kJ/mol
Best n = 1.000
DA Micropore Volume = 0.227 cc/g
Pore Diameter (mode) = 2.780e+00 nm or 2.78 nm

In the gas physisorption and surface area analysis, Best E and Best n are parameters generated when applying the DA model to the adsorption data (extracted alongside standard BET surface area reports). Best E represents the characteristic energy of adsorption (E), usually measured in kilojoules per mole (kJ/mol). It quantifies the thermodynamic favorability and strength of the interaction between the gas molecules (adsorbate) and your material's surface (adsorbent). It indicates whether the gas molecules are held loosely or tightly by the material's micropores. Typically, for low values (i.e., < 8–10 kJ/mol) is a pure physisorption process dominated by weak Van der Waals forces. This means the gas easily absorbs and desorbs [46, 47]. Higher values indicate a much stronger affinity or narrower micropores where the adsorption potentials from opposite pore walls overlap, drawing gas molecules in more strongly.

Best n (Astakhov Exponent / Heterogeneity Factor) is a non-integer empirical exponent (n) in the DA equation that reflects the structural homogeneity or pore-size distribution of the sample. It describes how uniform the adsorption energies are across the material's pore network [47]. Given: n = 2, the DA equation simplifies exactly to the standard Dubinin-Radushkevich (DR) equation. This typically indicates a homogeneous micropore structure with a Gaussian pore-size distribution; n = 1, which is often outputted by software when the material exhibits an incredibly uniform surface energy or highly specific localized site adsorption; n > 2 or non-integer values (e.g., 2.5, 3.4), strongly indicates structural heterogeneity (a broad or complex distribution of different pore sizes and shapes) [46, 47].

Barrett-Joyner-Halenda (BJH) Analysis

The BJH method uses the Kelvin equation to relate capillary condensation steps in the hysteresis loop to pore radius or diameter, and the following results was achieved:

Surface Area = 324.210 m^2/g

Pore Volume = 0.158 cc/g

Pore Diameter Dv(d) = 2.115 nm

Since the BJH confirmed what the DLS analysis showed – i.e., the bio-composites to be mesoporous (having average size ranging between 2–50 nm), the BJH model to the isotherm data is applicable [48, 49].

Pore diameter (or width) Vs Cumulative and Differential Pore Volume Plot

The plot of pore width (nm) on the horizontal axis against the cumulative and differential pore volume on vertical axis is shown in Figure 19:

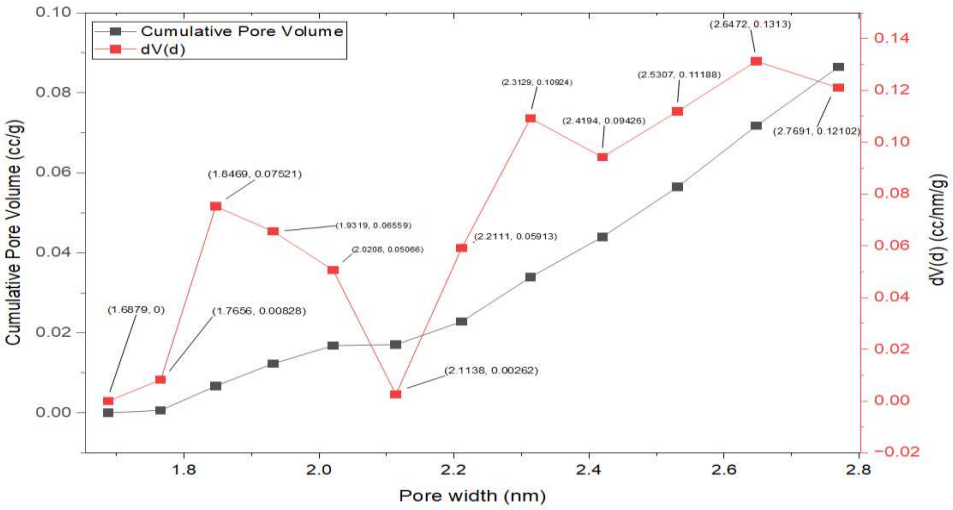

Figure 19: Pore diameter (or width) Vs Cumulative and Differential Pore Volume Plot

From Figure 19, the total pore volume added up as pore width increased. The curve starts at zero and rises until it flattens out at the maximum total pore volume. The flat-top part of the curve shows the total pore volume. Where the sharpest rise happens on the graph shows which pore size range holds most of the biocomposite volume.

The differential pore volume plot shows the change in pore volume for each specific pore width size (dV/dw) and turns the data into peak shapes. Each peak points to a dominant pore width size in the biocomposite. The tall, sharp peak means many pores share that exact size, while multiple peaks mean the biocomposite has a mixed range of pore sizes.

Pore diameter (or width) Vs Cumulative and Differential Pore Surface Area Plots

The plot of pore width (nm) on the horizontal axis against the cumulative and differential pore surface area on vertical axis is shown in Figure 20:

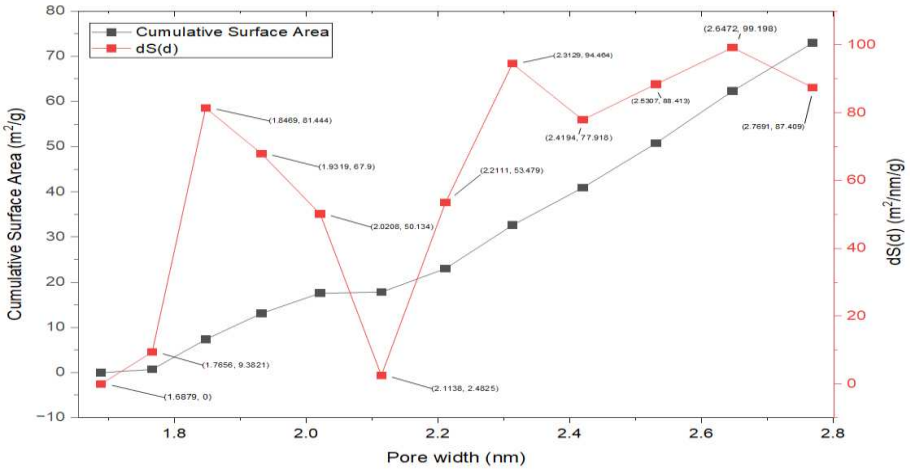

Figure 20: Pore diameter (or width) Vs Cumulative and Differential Pore Surface Area Plot

From Figure 20 plots total accumulated surface area (m^2/g) from a starting pore width up to a given pore width. The plateau (maximum value) on the far right gives the total BJH-derived pore surface area. The sharp vertical jump indicates that a massive portion of the biocomposite internal surface area comes from pores of that specific width range. Since the curve rises gradually across a wide horizontal span, surface area is contributed by a broad, heterogeneous range of pore sizes.

On the other hand, in the differential surface area with respect to pore size or incremental area per pore width interval) against pore width, each peak represents a dominant pore width (mode) that contributes the highest concentration or frequency of surface area. The sharp, narrow peak means uniform (monodisperse) pore dimensions; the broad peak or multiple peaks mean a multi-modal or highly irregular pore size distribution. The higher the peak, the greater abundance of pores within that specific narrow width window contributing to the surface area. Various analytical methods were employed in analyzing the surface area and volume of the biocomposite and is summarized below:

Area-Volume Summary

Analysis		
Sample Weight:		0.9g
Outgas Time:		3.0hrs
Analysis Gas:		Nitrogen (N_2)
Press. Tolerance:		0.100/0.100 (ads/des)
Analysis Time:		64.3 min.
Sample Volume:		1cc
Outgas Temp:		250.0 K
Bath Temperature:		273.0 K
Equil Time:		60/60 sec (ads/des)
Equil Timeout:		240/240 sec (ads/des)
Instrument:		Nova Station B

Data Reduction Parameters

Thermal Transpiration:		On
Eff. mol. diameter (D):		3.54 Å
Eff. cell stem diam. (d):		4.0000 mm
t-Method	**Calc. method:**	de Boer
BJH/DH method	**Moving pt. avg.:**	off
DR Method	**Affinity coefficient (β):**	0.3300
HK method	**Tabulated data Interval:**	1
SF method	**Tabulated data Interval:**	1
DFT method	**Cal. Model:**	N_2 at 77 K on Carbon (slit pore, NLDFT equilibrium model)
	Rel. press. Range:	0.0000 – 1.0000
	Moving pt. avg:	off
Adsorbate:	**Nitrogen**	
	Temperature:	77.350 K
	Molec. Wt.:	28.013
	Cross Section:	16.200 $Å^2$
	Liquid Density:	0.808 g/cc
	Critical Temp.:	126.200 K

	Critical Pressure:	33.500 atm
	SuperCritic. K.:	1.000
Adsorbent:	**Carbon**	
	DR. Exp (n):	2.000

Table 9: The Area-Volume Analysis Summary for the Adsorption Study of the Biocomposite

Parameter	Method	Quantity
Surface Area	SinglePoint BET	181.7 (m^2/g)
	MultiPoint BET	252.7 (m^2/g)
	Langmuir Surface Area	724.5 (m^2/g)
	BJH method cumulative adsorption surface area	324.2 (m^2/g)
	DH method cumulative adsorption surface area	346.2 (m^2/g)
	t-method external surface area	252.7 (m^2/g)
	DR method micropore area	297.0 (m^2/g)
	DFT cumulative surface area	729.7 (m^2/g)
Pore Volume	BJH method cumulative adsorption pore volume	0. 1580 (cc/g)
	DH method cumulative adsorption pore volume	0.1621 (cc/g)
	DR method micropore volume	0.1056 (cc/g)
	HK method micropore volume	0.05010 (cc/g)
	SF method micropore volume	0.01454 (cc/g)
	DFT method cumulative pore volume	0.08648 (cc/g)
Pore Size	BJH method adsorption pore Diameter (Mode Dv(d))	2.115 (nm)
	DH method adsorption pore Diameter (Mode Dv(d))	2.115 (nm)
	DR method micropore Pore width	5.651 (nm)
	DA method pore Diameter (Mode)	2.780 (nm)
	HK method pore Diameter (Mode)*	0.3675 (nm)
	SF method pore Diameter (Mode)*	0.4523 (nm)
	DFT pore Diameter (Mode)	2.647 (nm)

Heterogeneity of adsorption pore volume distribution affected adsorption and diffusion processes of spent engine oil and diesel by the nanobiocomposite in this various analysis. The BET and BJH methods are commonly used in adsorption characterization. The BET method is primarily used to measure the surface area of a material, while the BJH method is used to analyze the pore size distribution. However, it's important to note that the BJH method also provides surface area values in its results. The difference in surface area values obtained by the BET and BJH methods is due to the different approaches used in each test. The BET method

like the Dubinin-Radushkevich (DR) relies on physical adsorption of gas molecules on the surface of the material to calculate the active surface area [50]. On the other hand, the BJH method uses gas adsorption analysis to measure and analyze the pore volume and pore size distribution. The BET method is widely used for measuring surface area in scientific studies because it provides a good estimation of the active surface area and is considered more accurate. It is the recommended method for general surface area measurements. However, it is not suitable for accurately characterizing pores other than mesopores, which are pores with a size range of 2-50 nm. If your focus is on studying small or micropores, such as macropores or micropores, it is advisable to use the BJH method for a more precise analysis of pore size distribution. The BJH method can provide additional information about the distribution and volume of different pore sizes. In summary, the BET method is commonly used for surface area measurements due to its accuracy and widespread use in scientific research. However, in the case of studying small or micropores, the BJH method is recommended for a more comprehensive analysis of pore size distribution [50]. Saito-Foley (SF) and Horváth–Kawazoe (HK) methods, are analytical model derived for calculating pore size distributions in the micropore range (pores smaller than 2 nm), and inefficient for a wider range of application.

X- Diffractometry (XRD) Spectroscopic Analysis

The sample of powdered corncob and groundnut shell analyzed are amorphous based on the graph of intensity (cps) against diffraction angle (2θ) generated from XRD analysis. Amorphousness is characterized by lower, spread-out intensity peaks over 2θ – see Figures 21-23.

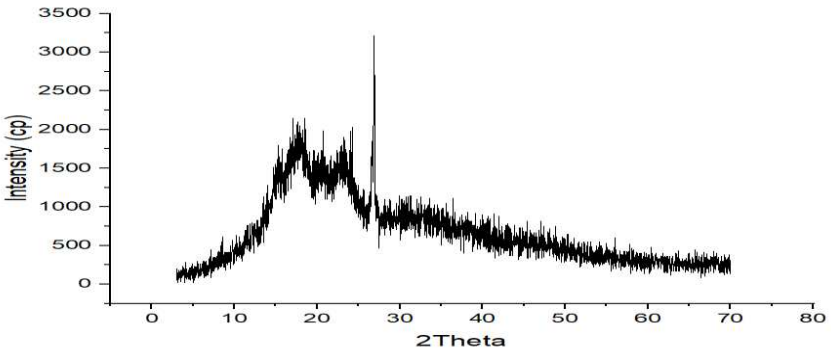

Figure 21: A raw plot of Intensity of light against angle of refraction, 2θ for Macro-sized Groundnut Shell and Corncob Biocomposite in 1:1 Mixture.

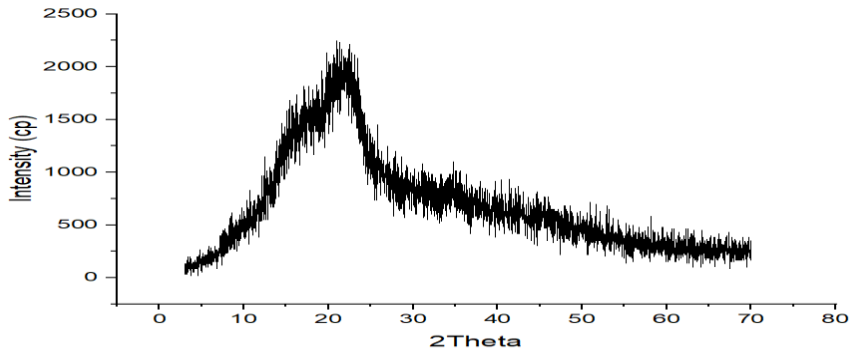

Figure 22: A raw plot of Intensity of light against angle of refraction, 2θ for Micro-sized Groundnut Shell and Corncob Biocomposite in 1:1 Mixture.

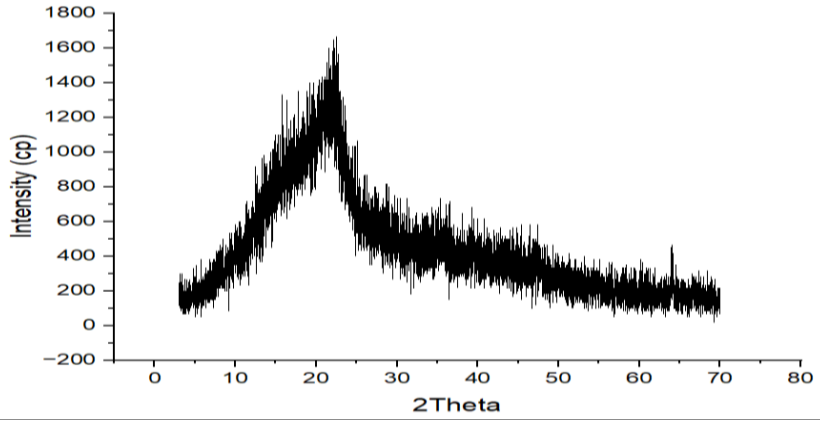

Figure 23: A raw plot of Intensity of light against angle of refraction, 2θ for Nano-sized Groundnut Shell and Corncob Biocomposite in 1:1 Mixture.

Figures 21, 22 and 23 show the refined phase data of the sample of macro, micro and macro sized corncob and groundnut shell biocomposite analyzed. Noticeably, there is a progressive change in peak intensity and broadness as milling time increases and biocomposite particle sizes decreases – from observed sharp peaks showing high definition in their structures from diffractions in XRD analysis, to broad and smoothly spread peaks across 2θ. This means that diffractions from the sample gradually become total reflection implying ordered long-range, periodic atomic arrangements within the sample gradually become disordered. The XRD analysis plot of results shown in Figures 21, 22 and 23 gives the various concentrations of constituents identified from XRD analysis – which is summarized in Table 10.

Table 10: Results XRD Analysis of Nanosynthesized Adsorbent

Particle Size	Component	Weight Fraction (%)
Macro	Quartz	43(10)%
	Orthoclase	27(7)%
	Osimilite	21(10)%
	Goethite	7.9(16)%
Micro	Chaoite	45.32(10)%
	Urea, syn	8.14(3)%
	Mascagnite	7.39(3)%
	Aluminium Phosphate	20.70(6)%
	Silicon Oxide	18.42(6)%
	Marialite	0.03(12)%
Nano	Chaoite	38.9(15)%
	Refikite	16.1(8)%
	Mascagnite	13.9(16)%
	Aluminium Phosphate	11.2(13)%
	Marialite	0.425(14)%
	Silicon Oxide	19.4(10)%

It is extremely unusual for raw, nanosynthesized corncob and ground nut shells to contain chemical compounds such as urea, shock-meteorite chaoite, or abattoir mascagnite. However, as a result of cross contamination, these chemical compounds tend to appear [51]. The accumulation of internal stresses and defects (dislocations) in the lattice resulted in peak shift form one angle of diffraction to another, changing 2θ positions that reflects changes in lattice spacing (*d*-spacing). High-energy milling of quartz produces amorphous silica (SiO_2) by breaking crystalline Si–O bonds. However, long-term milling has been noted to introduce foreign materials (such as SiO_2) from the milling media such as grinding balls or containers, which will appear as new, unexpected peaks in the XRD pattern [52-54]. Amorphous silica tends to have a higher adsorption capacity compared to crystalline silica due to its higher surface area, higher surface energy, and more disordered pore structure. These factors collectively enhance the availability of adsorption sites and the accessibility of molecules to those sites, leading to a greater adsorption capacity. Similarly, aluminium phosphate may exist in both crystalline and amorphous forms. The amorphous form (aluminium hydroxyphosphate) is characterized by a disordered atomic arrangement. On the other hand, crystalline aluminium phosphate has a well-defined crystal structure and can exist in various forms like berinite (similar to quartz), and tridymite-like or cristobalite-like structures depending on temperature. The surface characteristics from XRD analysis may suggest their adsorption ability, nonetheless there is need to also consider adsorption to typical molecules and interaction with materials such as spent engine oil and diesel in this study.

The experimental findings have shown that milling imparts mechanical energy that causes severe plastic deformation, particle fracturing, cold welding and generating effects which directly alter their crystal structure. With mechanical milling, crystallite size decreases leading to broadening of diffraction peaks. In addition, there is an evident decrease in intensity suggesting amorphization, with the crystal structure becoming increasingly disordered or amorphous (loss of crystallinity. This appeared as a decrease in peak intensity and an increase in background noise. Figure 24 and Table 11 highlights the outcome of continued milling.

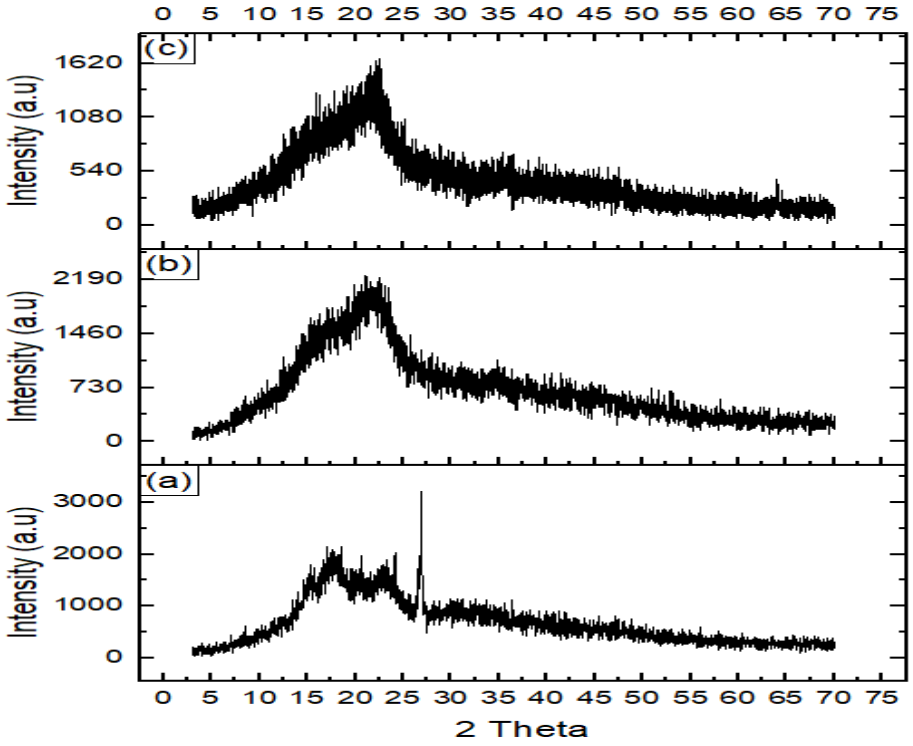

Figure 24: XRD plots of (a) Macro-sized sample, (b) Micro-sized and (c) Nano-sized Corncob and Groundnut shell biocomposite.

Table 11: Effect of Milling on Particle size

Feature	Short time/Initial milling	Extended/Long-term milling
Particle size	Decreases	Reaches nanoscale (~nm)
Peak Width	Slightly broadening	Significantly Broadens
Peak Intensity	High	Low (decreased crystallinity)
Structure	Crystalline	Amorphous/Nanocrystalline
Noise	Less	Increased

Measurement of Crystallinity from XRD

Using the method proposed by Segal *et al.* [49] and Nam *et al.* [50] where:

$$C.I\ (\%) = \left(\frac{I_t - I_a}{I_t}\right) \times 100\% \qquad (2)$$

Where, I_t and I_a are the total (of the 25.8° peak in Figure 17 and amorphous intensities respectively. However, the widely applied equation in determining the crystallinity of nanosynthesized corncob and groundnut shell is the Equation (3):

$$C.I\ (\%) = \left(\frac{A_c}{A_c + A_a}\right) \times 100\% \qquad (3)$$

Where, $C.I\ (\%)$ is the crystallinity index calculated in percentage, A_c is the area of the sharp crystalline peaks, and A_a is the broad amorphous halo, and $A_c + A_a$ is the total area under the region including the crystalline peaks and amorphous halo. From the analysis, we have: A_c= 7614.07739, and $A_c + A_a$ = 28115.44419 (given baseline constant (Y) = 16.6675):

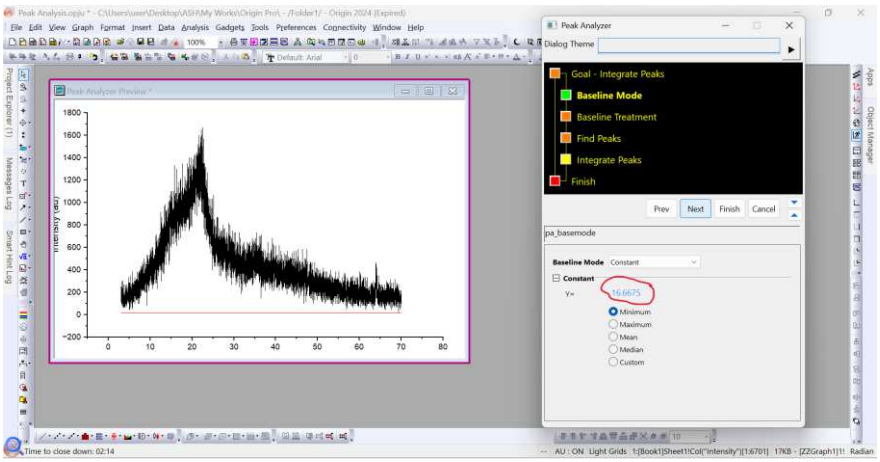

Figure 25: Shows a plot of Intensity against 2θ for XRD of Nano-sized GS and CC biocomposite given the baseline constant, Y = 16.6675 in the peak analysis.

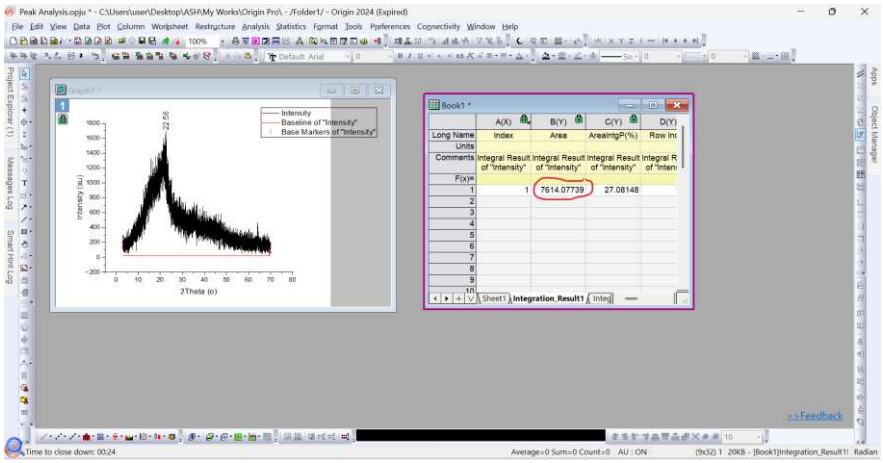

Figure 26: Shows a plot of Intensity against 2θ for XRD of Nano-sized GS and CC biocomposite given the that sharp crystalline peak location at 2θ = 22.56 and computed area of the crystalline peak = 7614.07739.

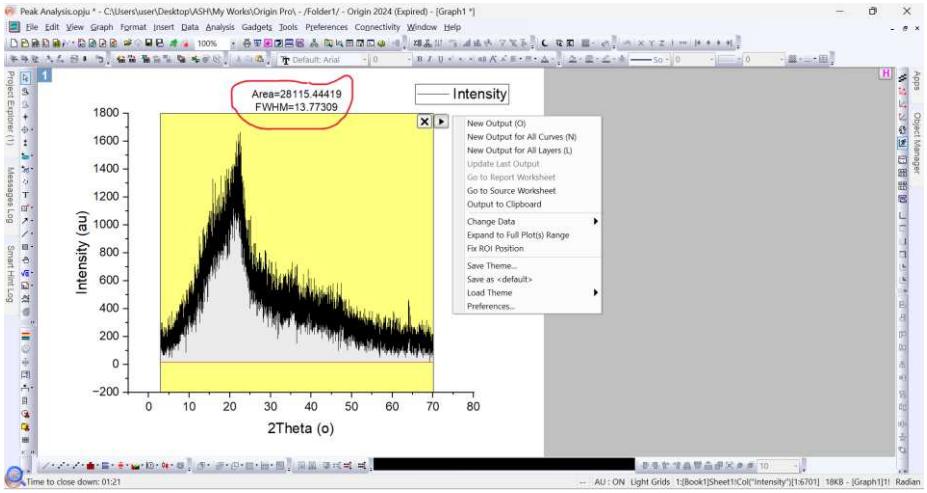

Figure 27: Shows a plot of Intensity against 2θ for XRD of Nano-sized GS and CC biocomposite given that the area of the under the graph = 28115.44419.

Hence, crystallinity Index for the nanosynthesized biocomposite is given as:

$$C.I\ (\%) = \frac{7614.07739}{28115.44419} \times 100\% = \ 27.081\%$$

Generally, a particle can be characterized as crystalline when its crystallinity index exceeds 50 – 60% [55, 56]. Hence, the biocomposite is amorphous in nature. A decline in CI is directly proportional to milling intensity and duration. Prolonged high-energy milling can reduce the CI of pure cellulose from around >70% down to near 0%, representing complete amorphization – energy-dependent decay. The mechanical milling of the cellulose-based biocomposite triggered a distinct structural transformation known as progressive amorphization. This process is characterized by a significant decline in Cellulose I crystallinity, which is typically quantified using the CI [57]. Table 12 highlights the surface and pore characteristics from the BET and XRD analysis of the three categories of particle sizes.

Table 12: Surface and pore structure of the precursors

Particle Size	BJH Pore size (nm)	DH Pore Volume (cc/g)	BET Surface Area (m^2/g)	Maximum RE (%)	FTIR Peak (Absorbance)	CI (%)
Nano	2.115	0.1621	**252.669**	**83.5**	**Higher**	**27.081**
Micro	0.025×10^6	0.3555	153.812	50.17	Moderate	34.211
Macro	$\mathbf{1.311\times 10^6}$	**0.5322**	105.322	16.23	Lower	46.320

Mechanical milling (such as ball milling, planetary milling, or jet milling) subjects the biocomposite to high-energy impact, shear, and compressive forces. The intense mechanical shear forces break down the highly ordered, hydrogen-bonded sheets of cellulose I which stabilizes its crystalline structure through a complex network of intra- and intermolecular hydrogen bonds. The kinetic energy from milling disrupts these bonds, causing the glucan chains to lose their periodic, parallel alignment by effectively peeling or fragmenting the highly crystalline core of cellulose microfibrils, converting them into a highly disordered, amorphous phase. As a result of milling time or energy increase, phase transformation is observed and the characteristic crystalline peaks of Cellulose I broaden and decrease in intensity, leading to a progressive decline in CI. Concurrently, the amorphous background becomes dominant.

Furthermore, the influence of the biocomposite matrix when milling a *biocomposite* rather than pure cellulose – such as the presence of the lignin/hemicellulose matrix polymer in natural fibers) altered the amorphization kinetics. A rigid, brittle matrix can help transfer mechanical stress more efficiently to the cellulose fibers, accelerating the decline in CI – shear transfer. Conversely, a highly ductile or elastomeric matrix may absorb a portion of the impact energy, acting as a cushion that slightly slows down the rate of cellulose amorphization and the creation of amorphous cellulose increases the available surface area and free hydroxyl groups, which can sometimes enhance interfacial bonding with the matrix upon co-melting or processing. Consequentially, amorphous cellulose becomes highly accessible – without the tight crystalline barrier, chemicals, enzymes, or solvents can easily penetrate the structure, significantly increasing its chemical reactivity or enzymatic digestibility; disordered glucan chains dissolve much more readily in cellulose solvents. While the amorphization yielded better matrix dispersion and reduced particle size, a drastic drop in Cellulose I crystallinity removed the rigid "reinforcement" effect. Over-milled cellulose lost its high tensile modulus, which can lead to a decrease in the overall mechanical strength of the final biocomposite and typically shifted the thermal decomposition onset of the biocomposite to a lower temperature range.

Adsorption Study of Adsorbent

Plot of time, *t* on horizontal axis against Removal Efficiency *R.E %* for the various size ranges of the adsorbent is shown below:

For Macro-sized (Average Particle Size > 100 µm): Figure 28 is a plot of R.E (%) on vertical Axis against Time (minutes) on horizontal axis of Macro-sized GS+CC (1:1) in spent engine oil and diesel-water emulsion at room temperature (31°C).

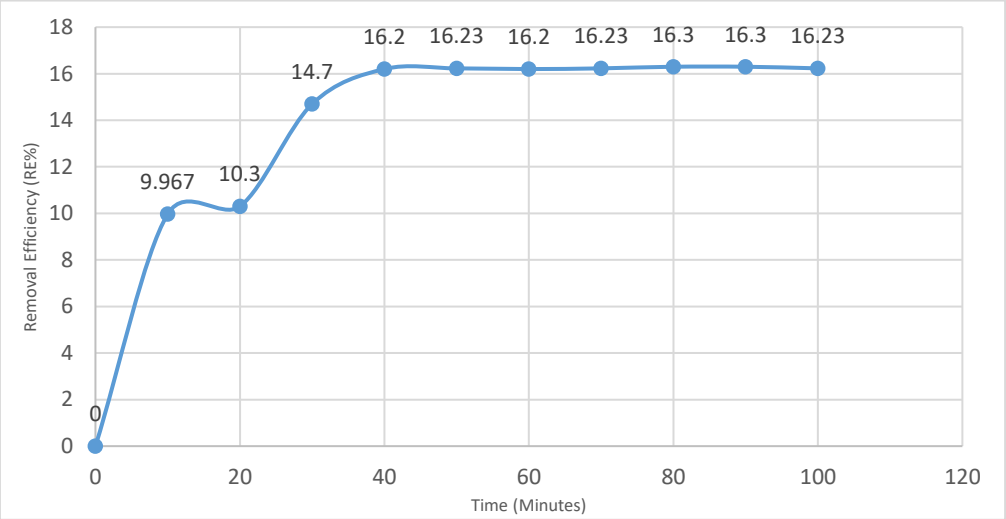

Figure 28: A plot of R.E (%) on vertical Axis against Time (minutes) on horizontal axis of Macro-sized GS+CC (1:1) in Spent Engine oil and Diesel-water Emulsion at room temperature (31°C).

For Micro-sized (Average Particle Size = 438.4 d.nm): Figure 29 is a plot of R.E (%) on vertical Axis against Time (minutes) on horizontal axis of Micro-sized GS+CC (1:1) in spent engine oil and diesel-water emulsion at room temperature (31°C).

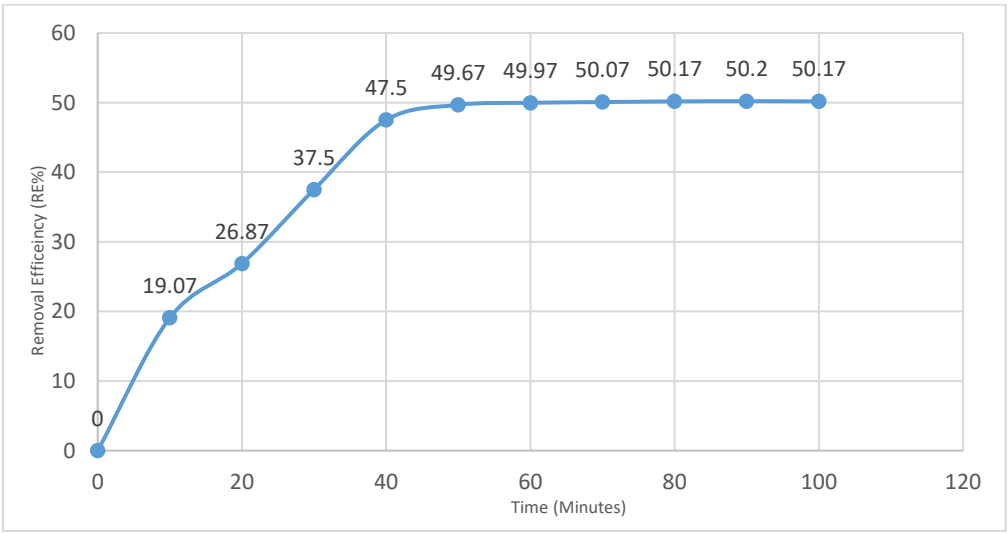

Figure 29: Plot of R.E (%) on vertical Axis against Time (minutes) on horizontal axis of Micro-sized GS+CC (1:1) in Spent Engine oil and Diesel-water Emulsion at room temperature (31°C).

For Nano-sized (Average Particle Size = 45.81 d.nm): Figure 30 is a plot of R.E (%) on vertical Axis against Time (minutes) on horizontal axis of Nano-sized GS+CC (1:1) in spent engine oil and diesel-water emulsion at room temperature (31°C).

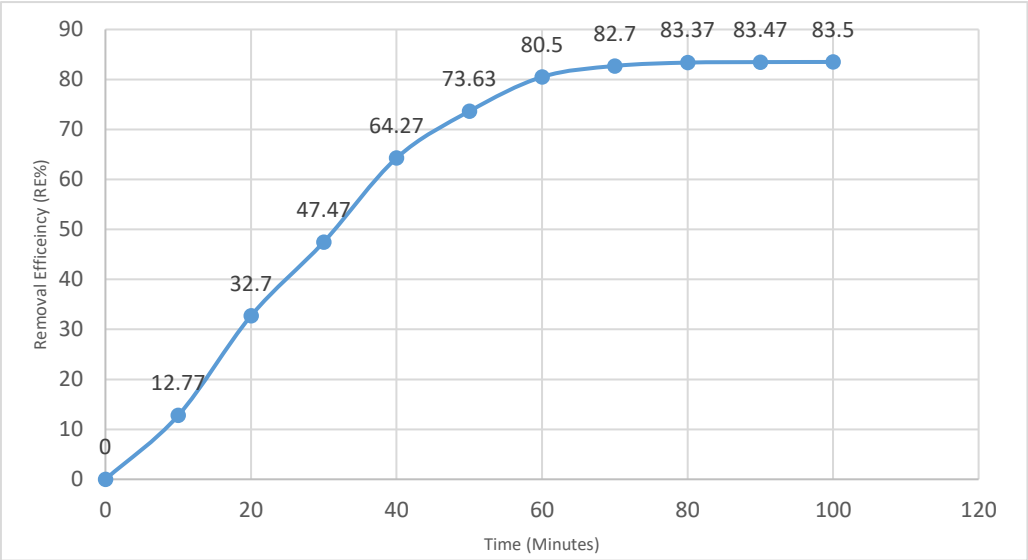

Figure 30: A plot of R.E (%) on vertical Axis against Time (minutes) on horizontal axis of Nano-sized GS+CC (1:1) in Spent Engine oil and Diesel-water Emulsion at room temperature (31°C).

Pollutant concentration at equilibrium can be obtained at the points on the graphs where the Removal Efficiency-Time line becomes a horizontal straight line. At, adsorption equals zero and beyond this point, with increasing time equilibrium is maintained or desorption may ensue if a negative concentration gradient is formed (i.e., if the concentration of the surrounding adsorbate becomes less than that of the adsorbent). It was observed that Macro-, Micro-, and Nano-sized particulates were attained at RE% of 16.2% (at about the 40th minute), 50.2% (at about the 70th minute) and 83.47% (at about the 90th minute) respectively. In addition, it can be seen from the data in Table 8, at the 10th minute of experimental study, Micro-sized particulates had higher RE% than Nano-sized particulates. This was as a result of the formation of a good number of coagulants of Nano-sized adsorbent in the adsorbate phase. The problem of coagulation was solved by rigorous agitation to achieve homogeneity of the mixture.

Mechanism of Adsorption using the Freundlich Adsorption Isotherm (FAI)

Table 13 highlights the experimental data of the isothermal process using macro, micro and nano-sized corncob and groundnut shell biocomposite as biosorbent in oil-water solution taking 60 mins as equilibrium time for each experiment replicated thrice (at 25°C room temperature).

Table 13: Experimental data of the isothermal adsorption study using Nano sized corncob and groundnut shell biocomposite as biosorbent in oil-water solution.

	S/N	1	2	3	4	5	6	7	8	9	10
	$C_{o(SE\&G)}$ (mg/L)	10	20	30	40	50	60	70	80	90	100
Macro-Sized	$C_{e\text{-}macro}$ (mg/L)	7.83	17.19	25.14	35.99	44.35	53.78	65.18	73.52	82.02	89.25
	$log\ C_e$	0.894	1.235	1.400	1.556	1.647	1.731	1.814	1.866	1.914	1.951
	$q_{e\text{-}macro}$	2.17	2.81	4.86	4.01	5.65	6.22	4.82	6.48	7.98	10.75
	$log\ q_{e\text{-}macro}$	0.336	0.449	0.687	0.603	0.752	0.794	0.683	0.812	0.902	1.031

Micro-Sized	$C_{e\text{-}micro}$ **(mg/L)**	4.83	13.21	15.01	28.68	37.73	46.51	55.85	60.75	62.21	65.44
	log C_e	0.684	1.121	1.176	1.458	1.577	1.668	1.747	1.784	1.794	1.816
	$q_{e\text{-}micro}$	5.17	6.79	14.99	11.32	12.27	13.49	14.15	19.25	27.79	34.56
	log $q_{e\text{-}micro}$	0.713	0.832	1.176	1.054	1.089	1.130	1.151	1.284	1.444	1.539
Nano-Sized	$C_{e\text{-}nano}$ **(mg/L)**	1.47	4.08	5.85	9.57	12.16	15.02	18.99	20.83	22.64	24.93
	log C_e	0.167	0.611	0.767	0.981	1.085	1.177	1.279	1.319	1.355	1.397
	$q_{e\text{-}nano}$	8.53	15.92	24.15	30.43	37.84	44.98	51.01	59.17	67.36	75.07
	log $q_{e\text{-}nano}$	0.931	1.202	1.383	1.483	1.578	1.653	1.708	1.772	1.828	1.875

NB: Concentration reported is the average from the experiments replicated thrice with a calculated standard deviation (≤ 8.84%) under the same conditions.

Figure 31 is the plot of log q_e on vertical axis against log C_{e-adsb} on horizontal axis using the data presented in Table 11.

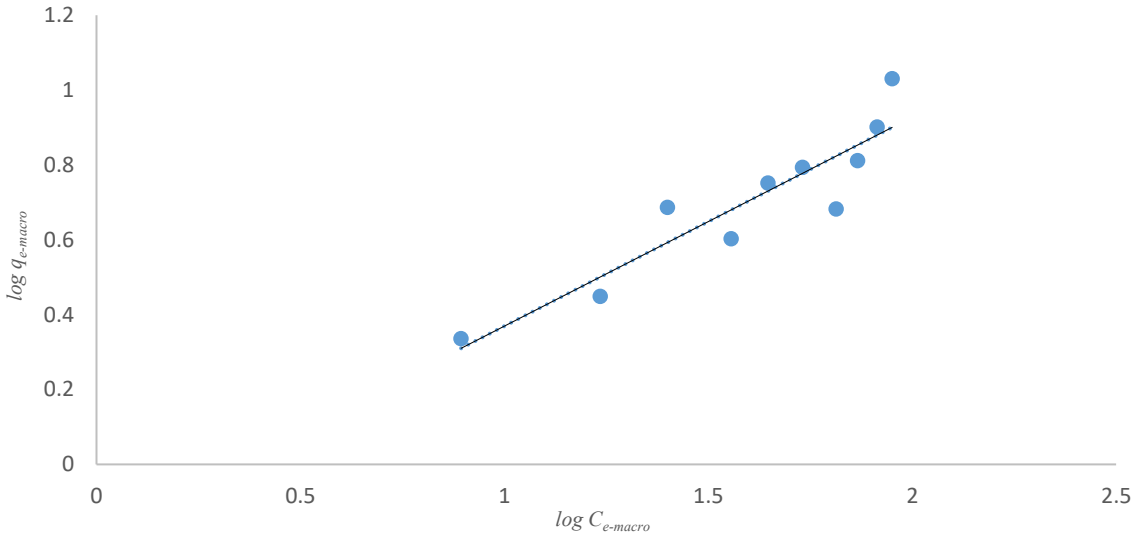

Figure 31: Shows the plot of log q_e on vertical axis against log C_{e-adsb} on horizontal axis for Macro-Sized GS and CC.

Given the line equation:

$$y = 0.5585x - 0.1891 \quad (4)$$

Given correlation coefficient $(R^2) = 0.8474$

Hence: $\log Q_e = \frac{1}{n}\log C_{e-adsb} + \log K_f$

Where, $\log Q_e = y$; $\log C_{e-adsb} =$ x ; $\frac{1}{n} = 0.5585$; and $\log K_f = -0.1891$.

Hence Equation (4) takes the form:

$$\log Q_e = (0.5585)\log C_{e-adsb} + (-0.1891) \quad (5)$$

Therefore, since $\log K_f = -0.1891$, then $K_f = 0.6470$. Also, given that $\frac{1}{n} = 0.5585$, then $n = 1.7905$. Where, $n > 1$ implies favorable adsorption.

Figure 32 is the plot of log q_e on vertical axis against log C_{e-adsb} on horizontal axis using the data presented in Table 11.

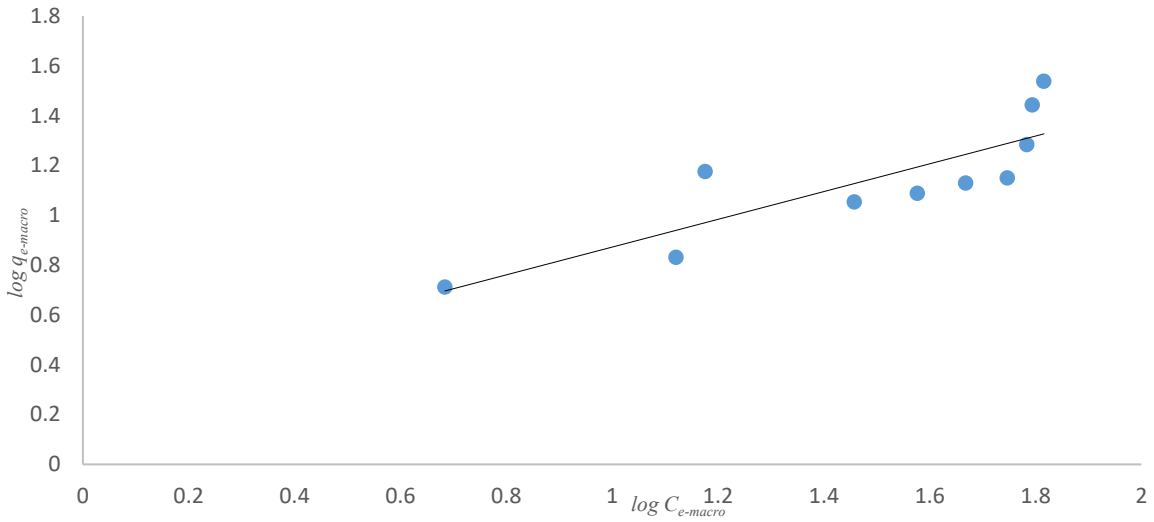

Figure 32: Shows the plot of log q_e on vertical axis against log C_{e-adsb} on horizontal axis for Micro-sized GS and CC.

Given the line equation:

$$y = 0.5574x + 0.3149 \quad (6)$$

Given correlation coefficient (R^2) = 0.7061

Factoring into Equation (6), we have that: $\log Q_e = \frac{1}{n}\log C_{e-adsb} + \log K_f$

Where, $\log Q_e = y$; $\log C_{e-adsb} = x$; $\frac{1}{n} = 0.5574$; and $\log K_f = 0.3149$.

Hence Equation (6) assumes the form:

$$\log Q_e = (0.5574)\log C_{e-adsb} + (0.3149) \quad (7)$$

Therefore, since $\log K_f = 0.3149$, then $K_f = 2.0649$. Also, given that $\frac{1}{n} = 0.5574$, then $n = 1.794$. Where, $n > 1$ implies favorable adsorption.

Figure 33 is the plot of log Q_e on vertical axis against log C_{e-adsb} on horizontal axis using the data presented in Table 11.

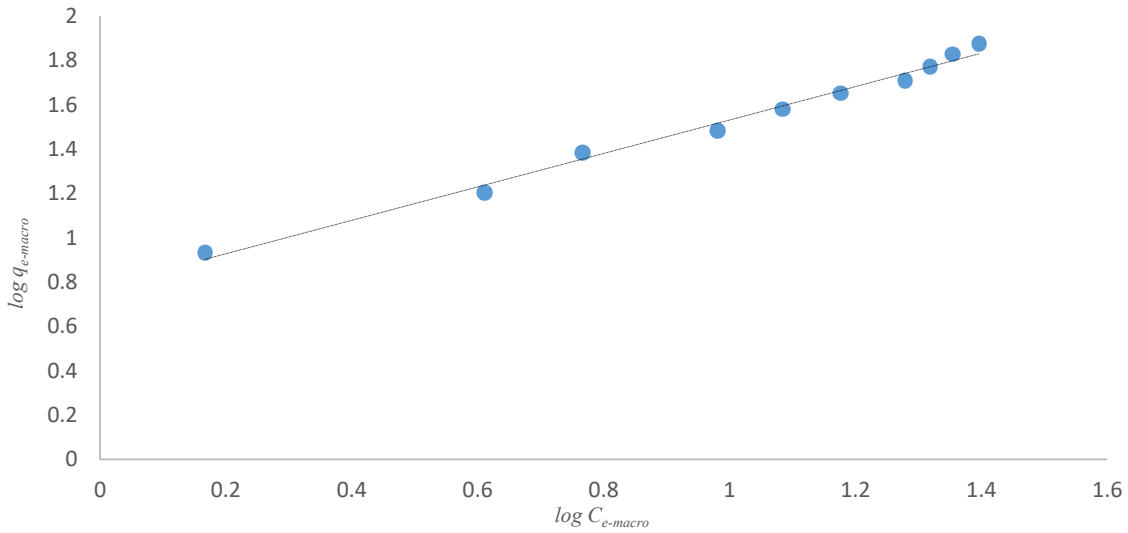

Figure 33: Shows the plot of log q_e on vertical axis against log C_{e-adsb} on horizontal axis for Nano-sized GS and CC.

Given the line equation:

$$y = 0.7541x + 0.7767 \quad (8)$$

Given correlation coefficient (R^2) $= 0.9896$

Factoring into Equation (8), we have that: $\log Q_e = \frac{1}{n}\log C_{e-adsb} + \log K_f$. Where, $\log Q_e = y$; $\log C_{e-adsb} = x$; $\frac{1}{n} = 0.7541$; and $\log K_f = 0.7767$. Hence Equation (9) assumes the form:

$$\log Q_e = (0.7541)\log C_{e-adsb} + (-1.6079) \quad (9)$$

Therefore, since $\log K_f = 0.7767$, then $K_f = 5.6768$. Also, given that $\frac{1}{n} = 0.7541$, then $n = 1.3261$. Where, $n > 1$ implies favorable adsorption.

While the study by Firdaus *et al.* [58] showed that adsorption is independent of the amount of adsorbent and can be used to determine the maximum adsorption capacity of the adsorbent, this study has shown that the surface chemistry of the adsorbent matters also in experimental cases such as this. Hence, the adsorption surface area directly determines the adsorption capacity of the material (as shown by $K_{f\text{-}nano}$ (5.6768) > $K_{f\text{-}micro}$ (2.0649) > $K_{f\text{-}macro}$ (0.6470)). While a higher K_f value indicates a stronger affinity of the adsorbent for the adsorbate, the *1/n* reflects the heterogeneity of the surface. A larger surface area provides more active sites for the adsorbate molecules to attach to, leading to a higher total amount of adsorption at equilibrium. This study backs up other studies that have shown that, the total surface area (S_{BET}) is proportional to the Freundlich capacity constant K_f; increasing S_{BET} roughly leads to a proportional increase in K_f under same conditions [59-63].

The Freundlich adsorption model is most suitable for describing physical, multilayer adsorption on heterogeneous surfaces with non-uniform active sites and varying sorption

energies. This phenomenon accounts for why a more disordered, heterogeneous surface, multilayered adsorption such as macro-sized and micro-sized corncob-groundnut shell biocomposite, have R^2 values (<0.9) (i.e. 0.8474 and 0.7061, respectively) compared to their nano-sized counterpart (having $R^2 = 0.9896$).

Compositional Analysis

Matched Findings of FTIR-ATR Results for Groundnut Shell and Corncob

Absorbance values of the analyzed peaks displayed a close trend of variation, which corresponds to the cellulose, hemicellulose and lignin content whose corresponding peaks assigned to functional groups from the works of Thota *et al.* [40] and Rosario *et al.* [64]. An FTIR-ATR was carried out on a 1:1 mixture of Groundnut Shell and Corncob as seen in Figure 34:

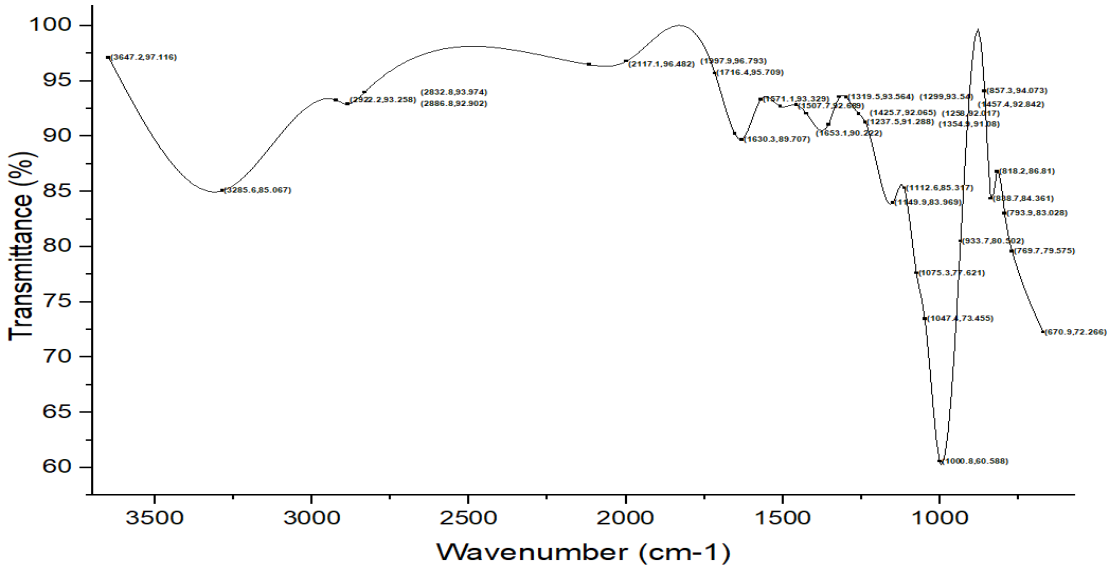

Figure 34: FTIR-ATR Results for Groundnut Shell and Corncob Mixture in 1:1 Ratio

Consistent with previous studies, both groundnut shell and corncob are lignocellulosic biomass materials containing substantial amounts of cellulose, hemicellulose, and lignin. Their structural components contribute to the chemical stability, biodegradability, and adsorption potential of the resulting biocomposite. Following the approach reported by Kostryukov *et al.* [65], the relative contributions of the major components was evaluated using calibration functions that related the intensity of characteristic absorption bands to the concentrations of lignin and cellulose in model samples. In this approach, lignin is associated primarily with the absorption band near 1512 cm^{-1}, while cellulose is represented by the band around 1450 cm^{-1}. The concentration of hemicellulose was estimated indirectly through its correlations with other structural components –from the chemometric analysis shown in Table 3. The reliability of this approach for determining the principal constituents of the synthesized adsorbent has also been demonstrated using the standard addition method and taking two major regions of consideration: 3902–2800 cm^{-1} and 1800–850 cm^{-1}.

The FTIR spectrum exhibited a broad absorption band at 3285.6 cm^{-1}, which can be attributed mainly to O–H stretching vibrations of hydroxyl groups present in cellulose and hemicellulose [66]. The presence of these hydrophilic functional groups suggests that the material possesses

considerable affinity for water and may contribute to its biodegradability [66–68]. Other characteristic absorption bands observed in the spectra correspond to functional groups associated with cellulose, hemicellulose, and lignin. These constituents are particularly important in determining the surface chemistry and adsorption behaviour of lignocellulosic materials. Their presence also supports the potential application of agricultural residues such as groundnut shell and corncob as naturally derived and environmentally compatible materials for composite adsorbents [34, 69]. The absorption peak at 1638.30 cm^{-1} may be associated with C=C stretching vibrations of aromatic structures, which are characteristic to lignin. The presence of lignin-containing aromatic structures can contribute to the structural stability and oil-adsorption capacity of the material [69]. Overall, the FTIR spectra indicate a considerable contribution of cellulose and lignin to the composite structure, reinforcing the suitability of corncob and groundnut shell as renewable, non-toxic, and potentially effective adsorbent materials [70].

The 3902–2800 cm^{-1} region contained characteristic bands associated mainly with O–H stretching and symmetric and asymmetric C–H stretching vibrations, functional groups are commonly associated with the hydroxyl-rich and aliphatic structures of lignocellulosic biomass. Within the fingerprint region (1800–850 cm^{-1}), several absorption bands were assigned to the principal structural constituents of the biocomposite. Cellulose-related bands occurred predominantly within approximately 990–1160 cm^{-1} and 1335–1440 cm^{-1}, while hemicellulose was associated with a band around 900 cm^{-1} [69-70]. Lignin-related absorption was observed near 1239.3 and 1375.4 cm^{-1}, reflecting vibrations associated with aromatic structures, while additional bands around 930, 1035, 1335–1440, and 3343 cm^{-1} are characteristic of functional groups associated with carbohydrates and lignin [71, 72].

The absorption bands at 1638.3 and 1541.3 cm^{-1} may be related to carbonyl-containing structures and vibrations associated with hemicellulose and extractive components, including esterified resin acids, waxes, and fats. Their relatively low absorbance (<0.10) in the biocomposite may be attributed to differences in the concentration or accessibility of these components. Extractive substances may also mask some of the characteristic vibrations of hemicellulose, thereby influencing the intensity of the corresponding absorption bands. Furthermore, the relatively weak definition of absorption features around 1600 cm^{-1} in the composite may be associated with other naturally occurring constituents, such as calcium oxalate and flavonoid compounds [69, 71, 72].

The spectral region between 1750 and 1510 cm^{-1} has previously been reported to contain absorption features that reflect variations in lignin and carbohydrate structures. Funda *et al.* [69], for example, identified chemical differences between juvenile and mature Scots pine wood based on vibrational features associated with lignin and carbohydrates. Similarly, Ozgenc *et al.* [73] demonstrated the potential of aromatic skeletal vibrations, particularly those occurring around 1508–1510 and 1603–1609 cm^{-1}, for assessing lignin content in alder and cedar. In the present study, the relatively pronounced absorption of bands associated with carbohydrate and lignin structures is consistent with the chemical composition previously reported for groundnut shell [69–75]. The spectral region between approximately 1510 and 1265 cm^{-1} may therefore provide useful evidence of the presence of lignin and carbohydrate-rich constituents, which are likely contributed substantially by the groundnut shell [76].

The carbohydrate-dominated region, extending from approximately 1200 to 890 cm^{-1}, also exhibited several prominent absorption bands, indicating a substantial contribution of polysaccharide components to the composite. According to Acquah *et al.* [77], characteristic

polysaccharide-related bands may occur near 897 cm^{-1}, 1030 cm^{-1}, 1157 cm^{-1}, and 1239 cm^{-1}. The band near 897 cm^{-1} can be associated with structural vibrations of cellulose, while the band around 1030 cm^{-1} may arise from C–H deformation in cellulose and C–O stretching vibrations in polysaccharides. The absorption near 1157 cm^{-1} is attributable primarily to C–O–C vibrations, whereas the band around 1239 cm^{-1} can be related to C–O stretching and in-plane O–H bending vibrations of polysaccharides [77]. Collectively, these spectral features confirm the lignocellulosic nature of the biocomposite and demonstrate the presence of abundant oxygen-containing and aromatic functional groups that may contribute to its physicochemical properties and adsorption performance.

The lignin component of both corncobs and groundnut shells provides a dense framework of aromatic rings and hydrocarbon structures. These groups (C-H, C-C, and C=C) act via hydrophobic interactions and Van der Waals (dispersion) forces. Because of the alike-pole-to-pole effect, the long, oily alkane chains in engine oil align and stick tightly to the hydrophobic, carbon-rich domains of the biomass. The -OH groups from the cellulose and hemicellulose that make up the vast majority of the biomass structure and in their raw state, these highly polar groups typically prefer water. However, engine oil contains performance additives (like detergents, dispersants, and anti-wear agents) that possess polar ends (i.e. polar heads). The OH groups on the biomass surface form weak hydrogen bonds and dipole-dipole interactions with these polar oil additives. However, raw hydroxyl groups are hydrophilic, and processing raw biomass into biochar via carbonization (pyrolysis) drives off these -OH groups, making the material much more hydrophobic and vastly improving its oil-retention capacity. Carboxyl (-COOH) and Carbonyl (C=O) groups are naturally occurring organic acids in the biomass fibers and oxidation sites on the surface. Similar to hydroxyl groups, the oxygen atoms in carboxyl and carbonyl functionalities interact with the polar components of the diesel and oil via electrostatic attractions. Used engine oil, in particular, undergoes thermal degradation and contains oxidized hydrocarbon fragments (like ketones and carboxylic acids) that naturally associate with the oxygen-containing functional groups of the adsorbent. Why it is a considerable phenomenon for a material to be amphipathic, this shows that the biocomposite can be selectively applied especially in programs that require spontaneous formation of stable barriers in water and in which water is a necessity for success – programs such as bioremediation.

It is noteworthy that while structure plays a vital role because a porous physical structure of the corncob–groundnut shell is important, these functional groups dictate the surface chemistry of the biocomposite. The grooves, macropores, and cracks act like microscopic traps, pulling the oil in via capillary action, where the nonpolar surface groups then lock the oil in place. Chemical treatments (like acetylation) can alter these functional groups to dramatically increase oil capacity. However, for processes that involve bioremediation and biosorption, where the goal is to use biomass as a natural, highly active sponge to capture, bind, or break down environmental pollutants such as spent-engine oil and diesel, acetylation may not be necessary because it blocks the exact chemical groups needed to trap pollutants [78-80], modifies the biomass cell wall, creating a physical and steric barrier [81, 82].

4.0 Conclusion

This study evaluated the effect of particle size, surface area, and functional chemistry on the adsorption of spent engine oil and diesel using corncob–groundnut shell bio-composites. Characterization results from DLS, BET, SEM–EDX, FTIR, and XRD analyses showed that mechanical milling reduced particle size, increased surface area, enhanced surface porosity,

and progressively transformed the material into a more amorphous structure. Adsorption performance improved significantly as particle size decreased. The nano-sized biocomposite achieved the highest removal efficiency (83.5%), followed by the micro-sized (50.2%) and macro-sized (16.2%) bio-composites. The superior performance of the nano-sized adsorbent was attributed to its larger surface area, greater pore accessibility, and increased availability of active adsorption sites. Freundlich isotherm analysis gave R^2 values of 0.8474, 0.7061 and 0.9896 for the macro-, micro- and nano-sized adsorbents, respectively, indicating the best fit for the nano-sized adsorbent. Overall, the results demonstrate that particle size reduction through mechanical milling is an effective strategy for enhancing the adsorption capacity of corncob–groundnut shell bio-composites. The findings confirm the potential of nanosynthesized corncob–groundnut shell bio-composites as low-cost, sustainable, and environmentally friendly adsorbents for the treatment of hydrocarbon-contaminated water. Future studies should focus on adsorption kinetics, regeneration and reusability, and application under real wastewater conditions.

References

[1] Yojana W, Shreya G, Sargar HB. Bioremediation of Petroleum Contaminated Soil. *Advances in Bioremediation and Phytoremediation for Sustainable Soil Management.* 2022;157-170. https://doi:10.1007/978-3-030-89984-4_10

[2] Sixtus EA, Abdullahi ME, Bala IA, Stephen Y, Zakari A. Application of Agricultural Wastes as Biostimulants in Petroleum Polluted Soil Remediation. *Conference Proceedings of the Nigerian Soc. Of Chem. Eng. 54th International Conference, Exhibition and Annual General Meeting, ABUJA* 2024, 13th – 16th Nov, pp. 207-217.

[3] Onuh CY, Dosunmu A, Anawe PAL, Okoro EE, Igwilo KC, Ehinmowo AB. The Rheological Behavior of a Pseudo-Oil-Based Mud Formulated with *Hura Crepitans* Plant Oil as Base Fluid. *Journal of Petroleum Exploration and Production Technology.* 2020; 10:71 – 89. https://doi.org/10.1007/s13202-019-0718-6

[4] Peng X, Mingbiao X. Damage Mechanism of Oil-Based Drilling Fluid Flow in Seepage Channels for Fractured Tight Sandstone Gas Reservoirs. *Geofluids*. 2019; 2672695: 1-15. https://doi.org/10.1155/2019/2672695

[5] Oto-Obong EO, Mohammed AE, Bala IA, Stephen Y, Sixtus EA. *Proceedings of the 1st Abuja International Engineering Conference (AIECO),* 2025; 1(1):1781-1780. ISBN: 978-978-699-065-1

[6] Ruchita D, Deepti M, Kuppusamy P, Udai BS, Asha S, Renu S, et al. Bioremediation of heavy metals from soil and aquatic environment: An Overview of Principles and Criteria of Fundamental Processes. *Sustainability*. 2015; 7: 2189-2212. https://doi:10.3390/su7022189

[7] Ashwini G, Basappa BK. Optimization of Nutrients Concentration Required for the Bioremediation of Petroleum Contaminated Soil. *International Research Journal on Advanced Engineering and Management*. 2024; 02(04): 1124-1134. https://doi.org/10.47392/IRJAEM.2024.0148

[8] Guwahati I. NPTEL: Contaminated site remediation. Available at https://nptel.ac.in/courses/105103025/20 accessed 12/12/2018. 2012.

[9] Mekonnen TA. A Review on Biodegradation and Biological Treatments of Cellulose, Hemicellulose and Lignin. Global Journal of Biology Agriculture and Health Sciences. 2021; 10(1):103. https://doi:10.35248/2319-5584.21.10.103

[10] Sixtus EA, Abdullahi ME, Bala IA, Stephen Y, Zakari A. Application of Agricultural Wastes as Biostimulants in Petroleum Polluted Soil Remediation. *Conference Proceedings of the Nigerian Soc. Of Chem. Eng. 54th International Conference, Exhibition and Annual General Meeting, ABUJA 2024, 13th – 16th Nov. 2024*, pp. 207-217.

[11] Paine RT, Jennifer LR, Adrian S, Elaine S, Marjorie JW, Christopher DGH, et al. Trouble on oiled waters: Lesson from the Exxon Valdez Oil Spill. *Annual Review of Ecology and Systematics*. 1996; 27(1):197-235. https://doi:10.1146/annurev.ecolsys.27.1.197

[12] Moghaddam M, Rahmani, Azizi F. Adsorption equilibrium in enzyme-substrate interactions. *Chemical Engineering Journal*. 2021; 173, 108201.

[13] William KG, Emik S, Öngen A, Kurtulus ÖH, Aydin S. Modelling of Adsorption Kinetic Processes – Errors, Theory and Application, Advanced Sorption Process Applications. *IntechOpen,* Feb. 20, 2019. https://doi.org/10.5772/intechopen.80495

[14] Singh, Kumar P, and Raj S. Competitive adsorption dynamics in protein interactions. *Journal of Molecular Biology*. 2020; 432(5), 1254–1263.

[15] Stefano M, Francesca C. Mechanisms of Soil Organic Carbon and Nitrogen Stabilization in Mineral Associated Organic Matter – Insights from Modelling in Phase Space. *EGUsphere.* 2024;1092. https://doi.org/10.5194/eguspere

[16] Kapoor M, Panwar D, Kaira GS. Bioprocesses for Enzyme Production Using Agro-Industrial Wastes: Technical Challenges and Commercialization Potential. *Apply and Exploit the Emerging and Valuable Use Options of Waste Biomass.* 2016; 3: 61-93. https://doi.org/10.1016/B978-0-12-802392-1.00003-4

[17] Sixtus EA. Genetic Engineering in Bioremediation of Petroleum Contamination: Opportunities, Challenges and Economic Implication. *LAP Lambert Academic Publishing.* 1: 1-71, 2024. ISBN-10 6207639928

[18] Gandam PK, Chinta ML, Gandham AP, Pabbathi NPP, Konakanchi S, Bhavanam A, et al. A New Insight into the Composition and Physical Characteristics of Corncob – Substantiating its Potential for Tailored Biorefinery Objectives. *Fermentation*. 2022; 8(12): 704. https://doi.org/10.3390/fermentation8120704

[19] Kevin JS, Benjamin NB, Richard EM, Paul JW. Comparison of wet and dry corn stover harvest and storage. *Biomass and Bioenergy.* 2007; 31(4):211-221. https://doi.org/10.1016/j.biombioe.2006.04.007

[20] Sunaina S, Prakash C, Aman J. Biomass Derived Carbon for Supercapacitor Applications: Review. *Journal of Energy Storage*. 2021; 39:102646. https://doi.org/10.1016/j.est.2021.102646

[21] Rubén LM, Daniela Z, Dörte BKR, Petr B. Cellulose and Hemicellulose Decomposition by Forest Soil Bacteria Proceeds by the Action of Structurally Variable Enzymatic Systems. *Scientific Reports*. 2016; 6: 25279. https://doi:10.1038/srep25279

[22] Elise P. Lignocellulose-Degrading Microbes Gives Plants New Life. *American Society of Microbiology.* 2022; https://asm.org/articles/2022/march/lignoellulose-degrading-microbes-gives-plants-new-life

[23] Mehdi EJ, Ganesh N, Fatemeh A, Behzad F, Ali A, Mohammad AK, et al. Structure, Chemistry and Physicochemistry of Lignin for Material Functionalization. *Springer Nature Applied Sciences.* 2019; 1:1094. https://doi.org/10.1007/s42452-019-1126-8

[24] Aiping L, Xiaojie Y, Qinghua J, Li C, El-Gasim Y, Fakayode O, Cunshan Z. Preparation and characterization of lignin-containing cellulose nanocrystals from peanut shells using a deep eutectic solvent containing lignin-derived phenol. *Industrial Crops and Products.* 2023; 195: 116415. https://doi.org/10.1016/j.indcrop.2023.116415

[25] Junjie Y, Yao Z, Jizhang W, Zhigang L, Tao Z, Pingping L, et al. Conversion of agricultural waste biomass resource into high-added-value composite and its potential for boosting synergistic removal of ammonia nitrogen in practical water. *Food and Bioproducts Processing.* 2025; 150: 240-251. https://doi.org/10.1016/j.fbp.2025.01.018

[26] Sharma R., Vaidya D, Kaushal M, Gupta A, Shavnam, Thakur C. Valorization of corn waste for hemicellulose extraction and xylitol production: Comparative study of different extraction methods. *Biofuels, Bioprod. Bioref.* 2025; 19: 1746-1764. https://doi.org/10.1002/bbb.2782

[27] Ayodele C. Role of Surface Functional Groups on the Adsorption Capacity of Carbon Nanomaterials in Nigeria. *Journal of Chemistry.* 2024; 3(1):1-11. https://doi.org/10.47672/jchem.1972

[28] Jelena B, Marijana KI, Jasmina A, Maja V, Snežana M, Aleksandra T. Adsorptive Behavior of Corn-Cob- and Straw-Derived Biochar for Polycyclic Aromatic Hydrocarbon Removal from Aqueous Systems. *Processes*, 2025; *13*(5), 1521. https://doi.org/10.3390/pr13051521

[29] Zhuoqi X, Haiwei G, Tao L, Wangqing Z, Xiaodong M. Regeneration of Washing Effluents for Remediation of Petroleum-Hydrocarbons-Contaminated Soil by Corncob-Based Biomass Materials. *ACS Omega,* 2019 4 (20): 18711–18717. https://doi.org/10.1021/acsomega.9b02651

[30] Roberto OMJ, Wendell K.SC, Filipe SB, Fabiane S, Gabriel FS, Brenda LPS, Eliane C, Daniel PS, Denise SR. Utilization of corncob as adsorbent to remove oil and grease from produced water. *Petroleum Science and Technology,* 2022; 41(31):1-16. https://doi.org/10.1080/10916466.2022.2060258

[31] Darlington N and Uchenna A. Adsorption of Crude Oil Using Meshed Groundnut Husk. *Chemical Product and Process Modeling*, 2010, 5(1). https://doi.org/10.2202/1934-2659.1433

[32] Kpea-ue ML, Temple AE, Ngior W. Comparative Performance Analysis of Corncob and Groundnut Shell-Derived Activated Carbon as Adsorbents for the Treatment of Oilfield Produced Water. *Journal of Petroleum and Mining Engineering*, 2026; 28(1). https://doi.org/10.21608/jpme.2026.478517.1263

[33] Egbo WM, Yaguo EBI. Corn Cob Compost Stimulated Bioremediation of Petroleum Hydrocarbon Polluted Soil. *International Journal of Engineering and Modern Technology (IJEMT)*. 2024; 10(7). https://doi:10.56201/ijcsmt.v10.no4.2024.pg212.221

[34] Sixtus EA, Abdullahi ME, Yetunde MA, Enumah A., Stephen Y. Bioremediation of Engine-Oil and Grease Polluted Soil Using Compost Manure, Finely Granulated Corncob and Blend Groundnut Shell. *Journal of the Nigerian Society of Chemical Engineers.* 2024; 39(2):123-142. https://doi:10.51975/243902011.som

[35] Fukushima K, Abbate C, Tabuani D, Gennari M, Camino G. Biodegradation of Poly (Lactic Acid) and Its Nanocomposites. *Polymer Degradation and Stability*. 2009; 94(10):1646-1655. https://doi.org/10.1016/j.polymdegradstab.2009.07.001

[36] Yaro SA, Olajide OS, Ferdinand A, Patricia P. Synthesis of groundnut shell nanoparticles: characterization and particle size determination. *The International Journal of Advanced Manufacturing Technology*. 2017; 91:1111-1116. https://doi:10.1007/s00170-016-9778-7

[37] Van SP, Robertson J. Systems of Analysis for Evaluating Fibrous Feeds. *Standardization of Analytical Methodology for Feeds*. 1979; 4:49–60. ISBN: 0-88936-217-3

[38] Gustavo S, Erik JP, David AS. Fire Testing Methods of Bio-Based Flame-Retardant Polymeric Materials. *Bio-Based Flame-Retardant Technology for Polymeric Materials.* 2022;1(1):61-95. https://doi.org/10.1016/B978-0-323-90771-2.00009-2

[39] George FH, José S. Back-to-Basics Tutorial: X-Ray Diffraction of Thin Films. *Journal of Electroceramics*. 2021; 47:141–163 https://doi.org/10.1007/s10832-021-00263-6

[40] Sai PT, Pradeep KB, Yadhu NG, Praveen VV, Meera P, Rajesh BD, et al. Innovative Consortia of Micro and Macro Fungal Systems: Cellulolytic Enzyme Production from Groundnut Shell Biomass and Supportive Structural Analysis. *Journal of Sustainable Bioenergy Systems.* 2018; 8:47-66 http://www.scirp.org/journal/jsbs

[41] Holder F, Raymond ES. Tutorial on Powder X-ray Diffraction for Characterizing Nanoscale Materials Cameron *ACS Nano.* 2019; 13 (7), 7359-7365 https://doi.org/10.1021/acsnano.9b05157

[42] Małgorzata W, Anna DM, Adam WM. Comprehensive Studies of Adsorption Equilibrium and Kinetics for Selected Aromatic Organic Compounds on Activated Carbon. *Molecules,* 2024; 29(9):2038. https://www.mdpi.com/1420-3049/29/9/203

[43] Adamu AR, Muhammad HS, Jakada Y, Nurudeen S. Effect of Adsorbent Dosage on the Kinetics and Isotherms of Lead (II) Removal from Aqueous Solution Using Corn Husk. *Arid Zone Journal of Engineering Technology and Environment,* 2025; 21(3):702-716. https://doi.org/10.63958/azojete/2025/21/3/003

[44] Nickolay VB, Ekaterina NK. Measuring liquid density in a system for ensuring uniformity of measurements. *Journal of the Belarusian State University Physics.* 2022;3:113-119. https://doi.org/10.33581/2520-2022-3-113-119

[45] Kreyling GW, Manuela SB, Qasim C. A Complementary Definition of Nanomaterials. *Nano Today.* 2010; 5(3):165-168. https://doi.org/10.1016/j.nanotod.2010.03.004

[46] Akemu AO., Obahiagbon K., Eghe AO. Optimum Biodiesel Production from Shea Nut Oil by Heterogeneous Catalyst Transesterification. *International Journal of Research and Innovation in Applied Science (IJRIAS),* 2026; Volume XI, Issue V. https://doi.org/10.51584/IJRIAS.2026.11050003

[47] Hasan AM, Xiao W, Harvey JP, Gregory SP, Ali S. Experimental methods in chemical engineering: Density functional theory. *The Canadian Journal of Chemical Engineering*, 2021; 99: 1885–1911. https://doi.org/10.1002/cjce.24127

[48] Sahar S, Daniel L, Andry R, Nassim S. Microstructure of Dry Mortars without Cement: Specific Surface Area, Pore Size and Volume Distribution Analysis. *Appl. Sci.*, 2023; *13*(9), 5616; https://doi.org/10.3390/app13095616

[49] Kai W, Fangkai Q, Shizhao Z, Yubo Z, He S, Tingting Y, Zhenyuan Q. Adsorption Pore Volume Distribution Heterogeneity of Middle and High Rank Coal Reservoirs and Determination of Its Influencing Factors. *Processes*, 2025; *13*(2), 429; https://doi.org/10.3390/pr13020429

[50] Scherdel C, Reichenauer G, Wiener M. Relationship between pore volumes and surface areas derived from the evaluation of N_2-sorption data by DR-, BET- and t-plot. *Microporous and Mesoporous Materials,* 2010; Volume 132, Issue 3. https://doi.org/10.1016/j.micromeso.2010.03.034

[51] Pinku CN, Amiya O, Shubhankar D, Minaxi S, Kandi S, Prakash KN, Baskaran SI. Biogeneration of Valuable Nanomaterials from Agro-Wastes: A Comprehensive Review. *Agronomy,* 2023; 13, 561. https://doi.org/10.3390/agronomy13020561

[52] Ankit G, Menno D, Chia-Ching H, Peter S, Katerina D. Photophysical properties of ball milled silicon nanostructures. *Faraday Discuss.* 2020; 222: 96-107. https://doi.org/10.1039/C9FD00105K

[53] Arash K. A report on Silicon Dioxide. *Journal of Environmental Analytical Chemistry*. 2021; 8(11):344. ISSN: 2380-2391

[54] Alawaye EO. Morphology and Elemental Study of Silicon Nanoparticles Produced Using a Vibratory Disc Mill. *Nanoscience and Nanotechnology.* 2015; 5(3): 57-63. https://doi.org/10.5923/j.nn.20150503.02

[55] Randis R, Djarot BD, Femiana G, Achmad AS. Isolation and Characterization of Microcrystalline Cellulose from Oil Palm Fonds Biomass using Consecutive Chemical Treatments. *Case Studies in Chemical and Environmental Engineering*. 2024; 9, 100616. https://doi.org/10.1016/j.cscee.2024.100616

[56] Phan THA, Doan MT. Closer Approach towards the Preparation of Cellulose and Microcrystalline Cellulose from Corn Husks. *Chemical Engineering and Technology.* 2024; 47(9), e202300379. https://doi.org/10.1002/ceat.202300379

[57] Josué DHV, José JCP, Silvia LVA, Claudia MM, Felipe CS. Changes of crystallinity index and crystallite sizenin cotton cellulose nanoparticles obtained by ball milling. *17th International Conference on Electrical Engineering, Computing Science and Automatic Control (CCE), Mexico City, Mexico.* 2020; November 11-13, https://doi.org/10.1109/CCE50788.2020.9299162

[58] Patiha MF, Sayekti W, Fitria R, Triana K. Freundlich Adsorption Isotherm in the Perspective of Chemical Kinetics (III): Isolation Method Approach. *IOP Conf. Series: Materials Science and Engineering.* 2020; 858**,** 012010. https://doi.org/10.1088/1757-899X/858/1/012010

[59] Shams K, Sidqi AA, Muhammad SK, Shirish P. Surfactant Adsorption Isotherms: A Review. *ACS Omega.* 2021; 6(48):32342-32348. https://doi.org/10.1021/acsomega.1c04661

[60] Kawthar AB, Berihun MN, Shiferaw RJ, Tigabwa YA, Muhammed RM. Adsorption of gases on heterogeneous shale surfaces: A review. *Journal of Petroleum Science and Engineering*. 2022; 109466. https://doi.org/10.1016/j.petrol.2021.109466

[61] Behnaz B, Seyyed MM, Maryam Z, Mehrorang G, Sonia B, Seyyed AH. Biosorption. *Interface Science and Technology.* 2021; 33:587-628. https://doi.org/10.1016/B978-0-12-818805-7.00003-5

[62] Pouran P, Ali T, Mohsen T, Mehrorang G, Sepahdar H. Fundamentals of adsorption technology. *Interface Science and Technology.* 2021;33: 1-70. https://doi.org/10.1016/B978-0-12-818805-7.00001-1

[63] Saied A, Setareh E. Adsorption Isotherms and Kinetics. *Interface Science and Technology.* 2021;33:445-509. https://doi.org/10.1016/B978-0-12-818805-7.00011-4

[64] Rosario JA, Jorge JD, Gaston ZID. Determination of hemicellulose, cellulose, holocellulose and lignin content using FTIR in Calycophyllum spruceanum (Benth.) K. Schum. and Guazuma crinita Lam. *PLoS ONE.* 2021; 16(10): e0256559. https://doi.org/10.1371/journal.pone.0256559

[65] Kostryukov SG, Matyakubov HB, Masterova YY, Kozlov AS, Pryanichnikova MK, Pynenkov AA et al. Determination of Lignin, Cellulose, and Hemicellulose in Plant Materials by FTIR Spectroscopy. *Journal of Analytical Chemistry.* 2023; 78: 718-727. https://doi.org/10.1134/S1061934823040093

[66] Victoria EO, Arinze LE, Tobechukwu CE, Ferdinand CC. Comparative Analysis of Alkaline-Extracted Hemicelluloses from Beech, African Rose and Agba Woods using FTIR and HPLC. *Heliyon.* 2022; 8(6):e09714. https://doi.org/10.1016/j.heliyon.2022.e09714

[67] Yousra B, Somia F, Fouad EM, Abdellatif B. Impact of Natural Degradation on the Aged Lignocellulose Fibers of Moroccan Cedar Softwoof: Structural Elucidation by

Infrared Spectroscopy (ATR-FTIR) and X-ray Diffraction. *Fermentation.* 2022; 8(12), 698. https://doi.org/10.3390/fermentation8120698

[68] Budi I, Made LB, Sutikno S, Ubaidillah U, Iwan Y, Asranudin A, et al. Impact of Alkali Treatment on the Mechanical, Acoustic, and Morphological Characteristics of Sustainable Oil Palm Frond Fiber Composites. *South African Journal of Chemical Engineering.* 2025;09:004 https://doi.org/10.1016/j.sajce.2025.09.004

[69] Funda T, Fundova I, Gorzsa A, Fries A, Wu HX. Predicting the chemical composition of juvenile and mature woods in Scots pine (*Pinus sylvestris L.*) using FTIR spectroscopy. *Wood Science Technology.* 2020; 54(2):289–311. https://doi.org/10.1007/s00226-020-01159-4

[70] Beata GŻ, Julita M. Biosorption: An Efficient Tool for the Separation, and Preconcentration, and Speciation Analysis of Trace Metals in Biological and Environmental Samples. *Handbook of Bioanalytics.* 2022; pp 1-22. https://doi.org/10.1007/978-3-030-63957-0_47-1

[71] Tomas F, Irena F, András G, Anders F, Harry XW. Predicting the chemical composition of juvenile and mature woods in Scots pine (*Pinus sylvestris* L.) using FTIR spectroscopy. *Wood Science and Technology*, 2020; 54:289–311. https://doi.org/10.1007/s00226-020-01159-4

[72] Zhou C, Jiang W, Cheng Q, Via BK. Multivariate Calibration and Model Integrity for Wood Chemistry Using Fourier Transform Infrared Spectroscopy. *Journal of Analytical Methods in Chemistry*. 2015; 1:1–9. https://doi.org/10.1155/2015/429846

[73] Özlem Ö, Sefa D, Süleyman K. (2017)Chemical analysis of tree barks using ATR-FTIR¨ spectroscopy and conventional techniques. *BioResources*. 2017; 12(4):9143–9151. https://doi:10.15376/biores.12.4.9143-9151

[74] Popescu M, Popescu MC, Singurel G, Vasile C, Argyropoulos DS, Willfor S. Spectral Characterization of Eucalyptus Wood. Applied Spectroscopy. 2007; 61(11):1168–1177. https://doi.org/10.1366/000370207782597076

[75] Xu F, Yu J, Tesso T, Dowell F, Wang D. Qualitative and quantitative analysis of lignocellulosic biomass using infrared techniques: A mini-review. *Applied Energy*. 2013; 104:801–809. https://doi.org/10.1016/j.apenergy.2012.12.019

[76] Chioma MO, Joseph TN, Michael OD, Samuel AI. Chemical, Thermogravimetric and Elemental Characterization of Nigerian Groundnut and Cowpea Shells for Sustainable Valorization. *Sustainable, Clean and Emerging Energy Technologies Conference, IOP Conf. Ser.: Earth Environ. Sci.* 2024; 1322 (012003). https://doi.org/10.1088/1755-1315/1322/1/012003

[77] Acquah GE, Via BK, Fasina OO, Eckhardt L G. Rapid Quantitative Analysis of Forest Biomass Using Fourier Transform Infrared Spectroscopy and Partial Least Squares Regression. *Journal of Analytical Methods in Chemistry*. 2016;1–10. https://doi.org/10.1155/2016/1839598

[78] Júlia M, Jaiber RL, Vagner B, Adilson RG, Michel B. Hemicellulose Biomass Degree of Acetylation (Natural Versus Chemical Acetylation) as a Strategy for Based

Packaging Materials. *BioEnergy Research*, 2024; 17(2):1-20. https://doi.org/10.1007/s12155-024-10734-7

[79] Gregory J. Kennedy, Michael J. Bowman, Kim L. Ascherl, Nancy N. Nichols and Badal C. Saha. Biomass Demineralization and Pretreatment Strategies to Reduce Inhibitor Concentrations in Itaconic Acid Fermentation by *Aspergillus terreus*. *Biomass*, 2024; *4*(4), 1122-1141; https://doi.org/10.3390/biomass4040062

[80] Pritam A, Abhishek S, Adrija G, Gunjan S, Kuheli B, Priyabrata M, Mukut C, Dipankar C, Tapas KG. Current Biomass Treatment Methods for Sustainable Energy Generation. *Chemistry Select* 2025; 10, 36: e01487. https://doi.org/10.1002/slct.202501487

[81] Prashant MAP, Sanna K, Maija T, Ewa JM. Acetylation of woody lignocellulose: significance and regulation. *Front. Plant Sci*. 2013 ; 4:118. https://doi.org/10.3389/fpls.2013.00118

[82] Jude CO, Edith BA, Victor OA, Friday GO. Thermodynamic pathway of lignocellulosic acetylation process. *BMC Chemistry*, 2019; 13:79 https://doi.org/10.1186/s13065-019-0593-8

Funding Declaration

This research study received no dedicated grant support or external funding and was self-funded using the author's personal resources.

Supplementary Files

This is a list of supplementary files associated with this preprint. Click to download.

- Tables.docx
- GraphicalAbsract.docx